

**4D PRINTING OF SMART, MULTI-FUNCTIONAL, FIBER REINFORCED
COMPOSITES**

by

ATAKAN ALKAN

Submitted to the Graduate School of Engineering and Natural Sciences in partial
fulfillment of the requirements for the degree of Master of Science

Sabanci University

December 2024

TITLE OF THE THESIS/DISSERTATION

APPROVED BY:

Prof. Dr. Bahattin Koç
(Thesis Supervisor)

Prof. Dr. Mustafa Bakkal

Asst. Prof. Dr. Serkan Ünal

DATE OF APPROVAL: /12/2024

© Atakan Alkan, 2024
All Rights Reserved

Atakan Alkan
MFG, M.Sc. Thesis, 2024
Thesis Supervisor: Prof. Bahattin Koç

ABSTRACT

4D PRINTING OF SMART, MULTI-FUNCTIONAL, FIBER REINFORCED COMPOSITES

ATAKAN ALKAN

MFG, M.Sc. Thesis, December 2024

Thesis Supervisor: Prof. Bahattin Koç

Keywords: 4D printing, smart materials, CFRCs, reusability, shape recovery

This thesis explores the use of Carbon Fiber Reinforced Composites (CFRCs) in additive manufacturing, focusing on their potential in advanced applications requiring high strength, reusability and responsiveness to external stimuli. The study addresses the challenges associated with the fabrication of CFRCs, specifically in relation to path planning during four-dimensional (4D) printing process. A continuous path planning algorithm is developed and applied to both hexagonal cellular and solid CFRC structures, optimizing fiber placement and ensuring efficient manufacturing. Several tests are conducted to evaluate the material properties, including energy absorption, shape recovery, shape fixity, reusability and electro-active responses. The results demonstrate that CFRCs exhibit improved performance in terms of mechanical strength, reusability, and 4D responsiveness, highlighting their suitability for use in advanced applications. The findings suggest that CFRCs offer significant potential for various industries, especially in scenarios requiring adaptability and multifunctionality. This research contributes to the growing knowledge on smart materials and 4D printing applications.

ÖZET

AKILLI, ÇOK FONKSİYONLU, KARBON FİBER TAKVİYELİ KOMPOZİTLERİN 4D BASKISI

ATAKAN ALKAN

MFG, M.Sc. Tez, Aralık 2024

Tez Danışmanı: Prof. Bahattin Koç

Anahtar kelimeler: 4D baskı, akıllı malzemeler, CFRC, yeniden kullanılabilirlik, şekil geri kazanımı

Bu tez, eklemeli imalatta Karbon Fiber Takviyeli Kompozitlerin (CFRC'ler) kullanımını inceleyerek, yüksek mukavemet, yeniden kullanılabilirlik ve dış uyarıcılara duyarlılık gerektiren ileri düzey uygulamalardaki potansiyeline odaklanmaktadır. Çalışma, özellikle dört-boyutlu (4B) basım ile üretilen CFRC'lerin üretimini ele almaktadır. Tez kapsamında, sürekli basım algoritmaları ile geliştirilmiş hücreli ve hücreli olmayan CFRC yapılarında fiber yerleşimini planlayarak kullanıma uygun bir üretim gerçekleştirilmiştir. Enerji soğurma, şekil geri kazanımı, şekil sabitliği, yeniden kullanılabilirlik ve elektroaktif tepkiler dahil olmak üzere çeşitli malzeme özellikleri değerlendirilmiştir. Sonuç olarak, CFRC'lerin bu özelliklerinin üstün performans sergilediği ve ileri düzey uygulamalar için potansiyel taşıdığı ortaya konmuştur. Elde edilen sonuçlar, CFRC'lerin özellikle çok işlevlilik gerektiren uygulamalarda kullanılabilirliğini göstermiştir. Bu çalışmadan elde edilen sonuçlar, akıllı malzemeler ve 4B basım uygulamaları alanlarına katkı sağlayacaktır.

Acknowledgements

I would like to sincerely thank my professor, Prof. Dr. Bahattin Koç, for his guidance and support throughout my journey. His patience, expertise, and encouragement have been invaluable in helping me learn a new field in my career and giving me chance to contribute to research on additive manufacturing.

Specially, I want to thank Ali Fallah, for teaching me so much and providing guidance on my research and academic life. We worked together effectively, and I am pleased that our efforts were allowing us to make a meaningful contribution to the field of additive manufacturing. Throughout this collaboration, he patiently guided me toward specific research topics and helped me to become familiar with additive manufacturing which was outside my area of expertise in my previous career.

I also want to thank my research group, especially Amin Ranjbar, for his collaboration and contributions. He carried out the entire material characterization process and helped me to obtain an important parameter (T_g) for my research.

*Dedicated to my lovely cat, Olay,
who has the heart of a predator and the soul of a flower.*

Table of Contents

1. INTRODUCTION	10
1.1. Importance of 4D Printing in Additive Manufacturing	10
1.2. Additive Manufacturing of Carbon-Fiber Reinforced Composites	11
1.3. Auxetic Structures as Energy Absorbers	12
1.4. Smart Materials and Applications of CFRCs	13
1.5. Objectives of this thesis	16
2. METHODOLOGY	17
2.1. Co-axial Additive Manufacturing	17
2.2. Machine Setup	19
2.3. Materials	21
2.4. Energy Absorption and Reusability Evaluation of CFRCs	22
2.5. Cold programming of CFRCs	25
2.6. Shape Recovery and Shape Fixity Evaluation of CFRCs	26
3. CONTINUOUS PATH PLANNING OF CFRCs AND FABRICATION	28
3.1. Continuous Path Planning of Hexagonal Cellular CFRCs	28
3.2. Continuous Path Planning of Solid CFRCs	35
4. COLD PROGRAMMING OF UNIT CELL PLA/TPU CFRCs	41
4.1. PLA/TPU Filament Material Characterization	41
4.2. Cyclic Cold Programming of Unit Cell CFRCs	45
4.3. Energy Absorption and Reusability Investigation of CFRCs	47
4.4. Shape Recovery and Shape Fixity Properties of Unit Cell CFRCs	58
5. CELLULAR CFRC STRUCTURES AS REUSABLE ENERGY ABSORBERS	61
5.1. Re-entrant Cellular Structures as CFRC Energy Absorbers	61
5.2. Energy Absorption Investigation of Cellular CFRCs with Different Inner Angle	63
5.3. Path Optimization for Structural Failures	64
5.4. CFRC Shape Recovery with Hot-water Heating	65
6. ELECTRO-ACTIVE RESPONSES OF CFRCs	66
6.1. Electro-active Properties of CFRCs	66
6.2. Joule Heating of CFRCs	67
6.3. CFRC Shape Recovery with Joule Heating	69
6.4. Gradual Joule Heating Concept	71
6.5. Resistive Sensor Applications of CFRCs	71
7. CONCLUSION	73
8. REFERENCES	75

List of Figures

Figure 1: Stimuli response representation of SMPs.....	14
Figure 2: SMP implementation for grasping [35].	15
Figure 3: Co-axial printing representation for out-of-nozzle (a), in-nozzle (b) impregnation. [40]	18
Figure 4: (a) Effects of the different Li-Lo ratios on carbon-fiber distribution, (b) CFRCs with different number of carbon-fiber filament inputs.....	18
Figure 5: Extruder modification and machine setup	19
Figure 6: Force-Displacement curve for energy absorption calculations.....	23
Figure 7: Cold programming cycles of auxetic unit cell and cellular structure	25
Figure 8: Illustrations of recovery methods: (a) Hot water recovery, (b) Joule heating	27
Figure 9: Hexagonal cellular paths with different parameters like edge length (L), inner angle (A), number of rows (η_r) and number of columns (η_c).	30
Figure 10: (a) Dimensions of the auxetic unit cell, (b) Top rendered view of the CFRC unit cell with carbon-fiber, (c) Layer height and total height of the CFRC unit cell design.....	30
Figure 11: D70, D90, D110 CFRC sample part designs	31
Figure 12: Fabricate auxetic unit cell (a), D70 (b), D90 (c) and D110 (d) sample parts	32
Figure 13: a) Conventional path, b) Crossed path, c) Modified path.....	32
Figure 14: Compression test images and Force-Displacement curves of cellular auxetic CFRCs which printed with conventional, crossed and modified path.....	33
Figure 15: Example implementations of Algorithm 2.....	37
Figure 16: Stress concentration around plate with hole subjected to uniform tensile forces [57]. ..	37
Figure 17: The proposed path planning approaches for plate with hole problem.....	39
Figure 18: (a) Tensile test for PLA and CFRC structures, (b) Force(N)-Strain(%) plot of different path planning approaches.....	39
Figure 19: DSC results for pure PLA, TPU, and PLA/TPU mixtures	42
Figure 20: DMA results for pure PLA and PLA/TPU mixtures.....	43
Figure 21: The recovered length comparison of PT (a) and CPT (b) samples after 5 cycles of programming-recovery.....	46
Figure 22: The cold programming of PT/CPT samples with 30% (a) and 50% (b) deformation	47
Figure 23: Force-displacement plots of PT and CPT samples under 30% deformation	48
Figure 24: Force-displacement plots of PT and CPT samples under 50% deformation	50
Figure 25: Effect of carbon-fiber reinforcement on densification	55
Figure 26: Shape recovery ratio of the samples at different programming deformation, a and b are for 30% deformation, c and d are for 50% deformation	58
Figure 27: Shape fixity ratio of the samples at different programming deformation, a and b are for 30% deformation, c and d are for 50% deformation.....	59
Figure 29: Average shape recovery (a,b) and fixity (c,d) ratios with standard deviation.....	60
Figure 30: Effect of loading on auxetic and non-auxetic structures [24].....	61
Figure 31: Compression test cycle of D70, D90, D110 CFRCs.....	63
Figure 32: Force-Displacement plots of CFRCs and energy absorption calculations.....	63
Figure 33: Common breakage locations of loaded auxetic cellular CFRCs	64
Figure 34: Hot-water recovery of D70, D90 and D110 samples over time	65
Figure 35: Equivalent circuitry representation of D110 CFRC sample part.....	66
Figure 36: Arduino Uno voltage divider schematic for resistance measurement.....	67
Figure 37: The thermal images of D70 (a), D90 (b), D110 (c) sample parts for 120 seconds	68

Figure 38: The thermal images of deformed D70 (a), D90 (b), D110 (c) sample parts	69
Figure 39: Shape fixity (R_f) and shape recovery (R_r) ratios of D70, D90, D110 CFRCs	70
Figure 40: Gradual Joule Heating thermal images of D70 CFRC	71
Figure 41: Force-Resistance-Displacement cellular CFRCs under compression	72

List of Tables

Table 1: Printing Parameter Set.....	20
Table 2: Comparison of mechanical properties of different printing paths	34
Table 3: The T_g ($^{\circ}\text{C}$) of the PLA/TPU mixtures by DMA and DSC tests	44
Table 4. Energy absorption analysis of PT (unreinforced) samples under 50% deformation.....	51
Table 5. Energy absorption analysis of CPT (reinforced) samples under 50% deformation.....	53
Table 6: Standard deviation values for PT10, PT20, PT30, CPT10, CPT20 and CPT30 samples...	54
Table 7: Reusability factors of PT and CPT samples	56
Table 8: Energy absorption calculations for CFRCs	63

1. INTRODUCTION

1.1. Importance of 4D Printing in Additive Manufacturing

The increasing demand for multifunctional smart systems has resulted in a higher need for microcontrollers, sensors, and actuators, which in turn has led to larger and heavier machine components. This creates technical and commercial challenges such as limited space, slower response times, and constraints in operating environments. To address these challenges, there is a growing need for lightweight, smart, load-bearing components with fewer parts and lower costs. Recent advancements in additive manufacturing (AM) technology, particularly three-dimensional (3D) printing, have enabled the production of functional components with complex geometries, customized designs, and improved material properties [1-5].

Industries such as biomedical, automotive, aerospace, textile, and wearables are increasingly transitioning from traditional manufacturing methods to additive manufacturing, also called 3D printing technologies. The 3D printing of stimuli-responsive materials has recently led to the development of "4D printing," where time is considered the fourth dimension. It's important to note that the printing process in 4D printing is the same as in 3D printing, with the key distinction being that 4D printing uses smart materials that are programmable and can transform when exposed to specific stimuli. While 4D printed structures have shown potential for applications like space-deployable components, their current use is limited to small, non-load-bearing parts due to the inadequate strength of existing 4D printed structures [6, 7]. The mechanical properties of 4D printed shape-memory polymers (SMPs) can be improved by blending them with elastic materials such as silicone elastomers, or by adding particles, short fibers, or continuous fibers. However, previous studies have shown that significant improvements in mechanical properties are only achieved with continuous fiber reinforcement [8-11].

1.2. Additive Manufacturing of Carbon-Fiber Reinforced Composites

The incorporation of continuous fibers significantly enhanced the mechanical properties of the structures, while adding short fibers resulted in only a slight improvement in mechanical behavior. The additive manufacturing (AM) of carbon fiber reinforced composites (CFRCs) allows for the creation of complex structures with controlled fiber content and orientation, all while reducing costs and production time compared to traditional methods such as resin transfer molding, filament winding, automated fiber/tape placement, and vacuum bagging, which require specialized molds and tools. In recent years, various studies have examined the impact of factors such as printing process parameters, fiber pre-impregnation, and post-processing on the mechanical properties of printed CFRC structures [9, 12-14]. However, these studies have largely focused on the mechanical performance of these structures, with less attention given to other functional aspects. Recently, a few studies have started to explore additional functionalities of 4D printed CFRC structures, such as self-sensing, shape morphing, shape recovery, and energy storage capabilities. These findings highlight the significant potential of 4D printed CFRCs as the next generation of smart, multifunctional structures. Despite this promise, the technology is not yet mature enough to fully address the challenges of real-world industrial applications, and further research is needed. Several review articles discuss the 3D printing of CFRCs, focusing primarily on the fabrication process, including preprocessing, printing, and post-processing, and their effects on the mechanical properties of CFRCs [9, 15, 16]. However, recent research does not cover the shape memory and reusability properties or other functionalities of these structures. This thesis seeks present to design, fabrication and validation of 4D printed smart CFRC structures, focusing on the manufacturing process, materials used, and potential applications across various industries. It also discusses the challenges and limitations and the applications of 4D printed smart multifunctional CFRC structures.

Another important aspect of fabrication of CFRCs is continuous path planning. The existing path planning algorithms often introduce discontinuities in material deposition, which pose

challenges for continuous fiber composite printing. Unlike standard extrusion based additive manufacturing processes, continuous fiber reinforcement requires an uninterrupted material deposition process to maintain mechanical integrity. Disruptions in extrusion can lead to variations in material properties and structural weaknesses, where tool retractions result in carbon-fiber breakages or separation from matrix material. Lee et al. [17] presented a novel toolpath generation method for high speed machining process. He proposed a spiral topology toolpath to continuously machine with the minimum cutter retractions during the machining processes. Continuous path-planning algorithms have also been explored for machining operations. Elber et al. [18] developed a C1 continuous toolpath method for five-axis pocket milling using circular and linear segments to ensure smooth transitions. The path was generated by creating circular segments of maximally inscribed sizes connected by the linear segments. To overcome problems related to discontinuous path, algorithms for continuous fabrication of cellular and solid structures are developed during this study.

1.3. Auxetic Structures as Energy Absorbers

Unlike conventional materials, auxetic structures exhibit a negative Poisson's ratio (NPR), meaning they expand laterally when stretched rather than contracting. This characteristic enables auxetic materials to provide enhanced impact resistance and energy dissipation properties, which is advantageous in applications such as automotive, medical and aerospace. Previous research has shown that auxetic structures, due to their deformation behavior, can absorb energy more efficiently than traditional structures, making them promising candidates for load bearing applications. The mechanical behavior and energy absorption capacities of certain auxetic structures, such as re-entrant, semi-rigid, chiral, star, and arrowhead designs, have been the subject of in-depth study [19-21]. For example, Li et al. investigated the mechanical response of re-entrant auxetic structures to compressive loads, finding that changes in cell shape may have a considerable impact on the structure's mechanical

characteristics and Poisson's ratio [22]. Their findings showed that buildings with NPR had better energy absorption and lower transmitted stress than those with positive Poisson's ratios. Studies have demonstrated that the effectiveness of an energy absorber is often quantified by properties such as energy absorption efficiency, total absorbed energy and densification point, where the structure experiences substantial compression and its mechanical loading rises significantly [23-26]. These properties are essential to determine the suitability of a material or structure for energy absorber applications, and the unique deformation characteristics of auxetic structures allow them to achieve high energy absorption with relatively low weight. Also, with using auxetic geometries, it becomes possible to fine-tune energy absorption behavior and deformation behavior, enabling specific design adaptations for various applications [11, 13, 15].

1.4. Smart Materials and Applications of CFRCs

Smart materials, also known as stimuli-responsive materials, have the distinct capability to respond to external physical or chemical stimuli in a controlled and functional way. This ability allows them to carry out predefined tasks and adapt to their surroundings in ways that traditional materials cannot. The behavior of smart materials is directly influenced by the stimuli they encounter, such as light, electric and magnetic fields, pressure, heat, mechanical strain, or moisture [27, 28]. These stimuli act as triggers that cause the material to transform or respond functionally. For instance, changes in temperature can activate smart materials, prompting them to return to their original form after being deformed [29, 30]. An example representation of stimuli response mechanisms could be seen in *Figure 1*.

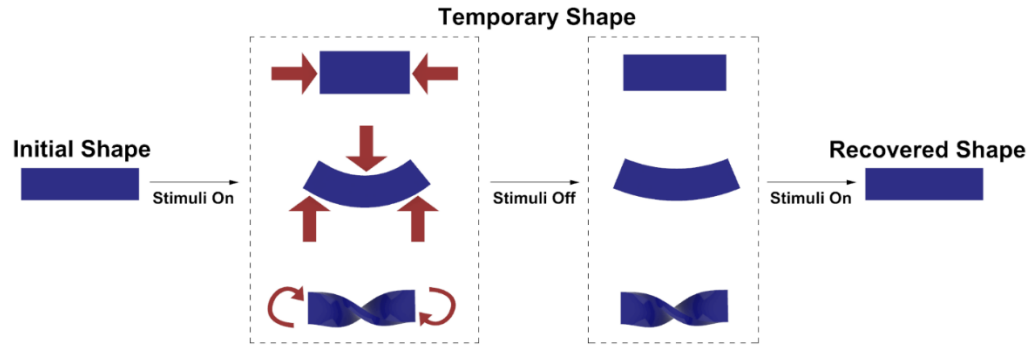


Figure 1: Stimuli response representation of SMPs

Among smart materials, two key categories stand out: Shape-Changing Materials (SCMs) and Shape Memory Materials (SMMs). SCMs can bend, twist, fold, or expand in response to stimuli and revert to their initial shape once the stimulus is removed [31]. In contrast, SMMs have a "memory" ability, allowing them to return to their original shape after being deformed, when exposed to specific stimuli like heat. These materials are vital in fields like aerospace and medical devices, where their response to external forces offers significant functional advantages [13, 31, 32]. Shape Memory Polymers (SMPs) are especially suitable for 4D printing because of their light weight, biocompatibility, and capacity for large deformations. These polymers can maintain a temporary shape and revert to their original form when triggered by external stimuli.

With advancements in Shape Memory Polymers (SMPs), programmable materials are emerging as the next step in the development of smart materials. These materials are engineered to alter their shape, properties, or functionality in response to external stimuli. Unlike traditional materials that passively adjust, programmable materials actively reconfigure, offering enhanced control over their behavior and applications. One of the most promising features of programmable materials is their ability to switch between different states, enabling dynamic products that can be reprogrammed for a variety of tasks [12, 33, 34].

Additive manufacturing (AM) has transformed the production of smart materials by providing greater control over both material properties and geometries. In contrast to traditional subtractive manufacturing processes, AM constructs objects layer by layer,

allowing for the creation of complex designs and the integration of multifunctional capabilities into a single component. This approach is particularly beneficial for smart materials, as it enables precise control over how materials respond to external stimuli, enhancing their overall performance. Precise control over the material broadens usage areas of SMPs like grasping end-effector implementation in *Figure 2* [35].

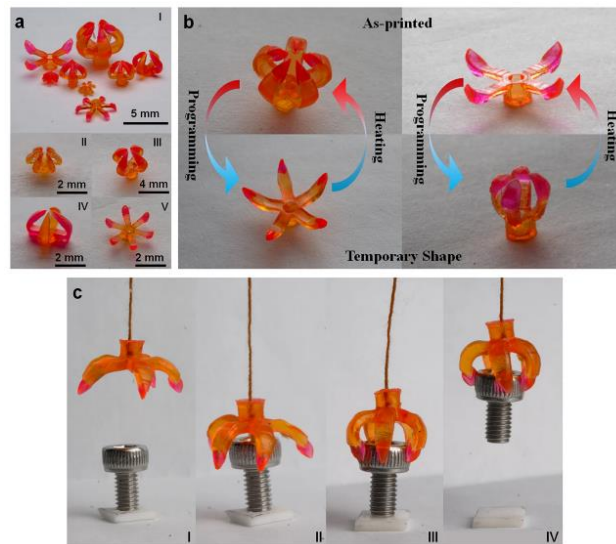


Figure 2: SMP implementation for grasping [35].

A significant advantage of using additive manufacturing for smart materials is the ability to customize material structures. For example, SMPs and other smart materials can be printed with specific geometric patterns that optimize their functional responses, such as deformation, conductivity, or energy absorption. Furthermore, the flexibility of AM allows for the incorporation of multiple materials into a single build, creating composite smart materials that can simultaneously respond to various stimuli [13, 36].

The increasing emphasis on sustainability has made smart materials essential in the development of eco-friendly technologies. Their ability to adapt and perform effectively under diverse conditions not only increases the longevity of products but also lessens the need for energy-demanding processes. A particularly promising feature of smart materials in this context is their use in self-healing technologies [37-39]. These materials are designed to automatically repair damage caused by wear and tears. In industrial settings, this can significantly reduce the need for maintenance, repairs, and replacement of damaged parts,

thereby decreasing resource consumption and waste. By improving the durability and lifespan of products, self-healing materials directly support sustainability initiatives by reducing the frequency of new component production and minimizing overall environmental impact.4D Printing of Smart Multifunctional CFRCs

1.5. Objectives of this thesis

The primary objective of this thesis is to explore the potential of 4D printing in advancing additive manufacturing processes, particularly in the context of Carbon Fiber Reinforced Composites (CFRCs). By addressing the integration of smart materials and innovative manufacturing techniques, this research aims to show potential of uses CFRCs in various applications.

In *Section 2*, designing a machine setup and material characterization to co-extruded materials in CFRCs and optimization of process will be discussed. Also, formulations for energy absorption calculation and cold programming will be discussed. One of the key challenges in fabrication of CFRCs, path planning will be addressed using continuous path planning algorithms in *Section 3*. Also, different path planning approaches for different use cases will be evaluated. In *Section 4*, cold programming of CFRCs will be implemented and shape memory and recovery capabilities of CFRCs will be examined in terms of energy absorption and reusability. In *Section 5*, cellular CFRC structures will be examined. And at the end, in *Section 6*, electro-active behavior of the CFRCs will be studied.

The use of CFRCs in advanced applications will be demonstrated with tests and verifications. The results showed that CFRCs are ideal for applications requiring high strength, reusability and responsiveness to external stimuli. By analyzing their performance in test scenarios, multifunctionality of the CFRCs will be remarked. Through these objectives, this thesis seeks to contribute to the field of additive manufacturing by expanding the applicability and functionality of CFRCs as smart materials.

2. METHODOLOGY

2.1. Co-axial Additive Manufacturing

Despite its numerous advantages, the extrusion based additive manufacturing processes present certain limitations, particularly concerning the mechanical properties of the printed parts. Since extrusion based additive manufacturing processes primarily rely on thermoplastic polymers as raw materials, the resulting components often exhibit lower strength and stiffness compared to traditionally manufactured parts. This makes these processes less suitable for high-load applications, restricting its use to prototyping, concept modeling, and functional parts [34]. One of the promising solutions to overcome these challenges is reinforcing the extruded material with other materials like continuous carbon fiber. There are three methods to impregnate continuous carbon-fiber in to extruded polymer. These are in-nozzle impregnation (in-situ), out-of-nozzle impregnation (dual extruder), and printing of pre-impregnated fiber method. The most simple and common method for continuous carbon-fiber reinforcement is the in-situ impregnation method (*Figure 3b*), where the matrix material and continuous reinforcing fibers fed separately to the extruder [40, 41]. The matrix was molten by the extruder heater and the reinforcing fibers were impregnated with polymer to execute extrusion. In the out-of-nozzle impregnation (*Figure 3a*), the thermoplastic matrix filament and the reinforcement fiber are extruded separately from two nozzles. In the third method, a continuous fiber-reinforced filament is fed to the extruder, and the impregnation is already done during the filament preparation (*Figure 3c*). During this study, in-nozzle impregnation is used for co-axial printing of CFRC structures.

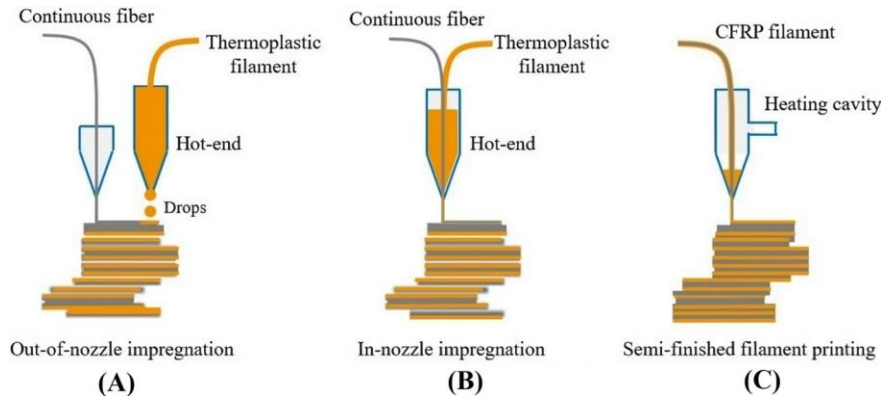


Figure 3: Co-axial printing representation for out-of-nozzle (a), in-nozzle (b) impregnation. [40]

The flow rate of the co-extruded material (ex. PLA or TPU) is highly correlated to printing quality of the structure. Because carbon fiber filament has a lower elongation capacity compared to the melted polymer, the printing speed and flow rate must be carefully aligned within a specific range during the printing process. This behavior arises from the pulling mechanism of the carbon fiber within the extruder head. Ideally, during the co-extrusion process, the unmolten material draws the carbon fiber into the feeding tube, preserving its integrity and physical form. However, if the printing speed exceeds the material feed rate, the printed structure on the heat bed begins to pull the carbon fiber directly instead of relying on material friction. This leads to structural breakages and discontinuous carbon fiber placement. *Figure 4a* illustrates the resulting discontinuities in the carbon fiber placement. The material feed rate is adjusted based on the length of the unmolten material entering the extruder head. For an output printed length L_o and an input material length L_i , L_i is set to a slightly lower value. Conversely, if L_i is set higher than L_o , the carbon fibers begin to spread out, resulting in random fiber placement within the co-extruded material.

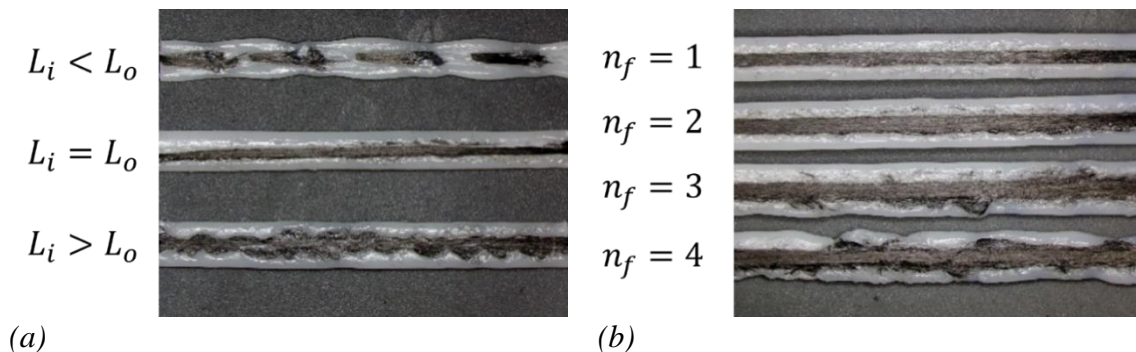


Figure 4: (a) Effects of the different L_i - L_o ratios on carbon-fiber distribution, (b) CFRCs with different number of carbon-fiber filament inputs

To increase the volume fraction of carbon fiber in the extruded material, varying the number of carbon fiber filaments, denoted as n_f , can be utilized. When $n_f=1$, the carbon fiber volume fraction is 2.5%. The printed results for different n_f values are shown in *Figure 4(b)*. It is observed that while the volume fraction can be increased, this comes at the expense of reduced printing quality due to extrusion challenges. With a nozzle diameter of 2 mm, the material extrusion rate is limited, making it insufficient to accommodate higher n_f values effectively.

2.2. Machine Setup

In order to enable the fabrication of carbon-fiber composite structures (CFRCs) with shape memory polymers (SMPs), a series of modifications were made to the Ender 3 V2 3D printer. This popular, cost-effective printer was adapted to handle the co-extrusion of carbon fibers and polymer filaments. The primary modification involved the integration of a carbon fiber feeding mechanism. To achieve this, an additional inlet hole was drilled into the filament feeding tube, allowing carbon fibers to be fed directly into the printer's hot-end during the printing process. (*Figure 5*) This adjustment enables simultaneous extrusion of the polymer filament and carbon fibers, creating a co-extruded composite structure. Such an approach is widely used in composite material manufacturing to enhance the mechanical strength and functionality of the printed parts, as demonstrated in previous research [16, 42, 43].

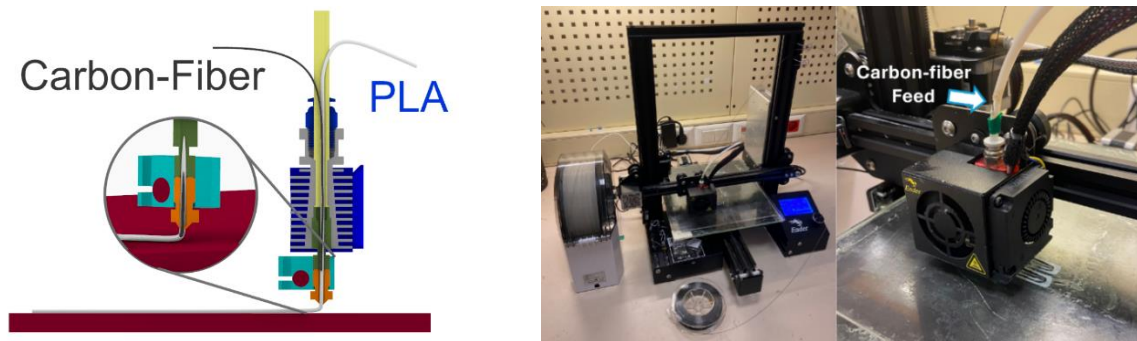


Figure 5: Extruder modification and machine setup

In addition to the filament feed modification, the printer's nozzle was enlarged from its standard diameter of 0.4 mm to 2 mm using a vertical drilling machine. The larger nozzle is essential to accommodate the increased volume of material and ensure smooth extrusion of the carbon fiber and polymer mixture. Without this modification, the smaller nozzle would be prone to clogging and insufficient material flow, leading to printing defects.

As previously described, modified 3D printer is used for continuous feeding of carbon fibers into the molten PLA matrix. To achieve optimal sample production, several printing parameters were calibrated through multiple trials. Process parameters were determined through iterative testing to achieve continuous fiber deposition and uniformity in the composite structure. Key parameters, such as nozzle temperature and printing speed, were optimized to prevent fiber buckling and ensure consistent bonding with the matrix. The resulting samples were analyzed for surface quality, structural integrity, and dimensional accuracy. The uniformity and surface finish of the printed layers confirmed the effectiveness of the calibrated parameters. The finalized parameter set (*Table 1*) are used for fabrication of CFRC samples. These parameters also compared with previous studies about co-axial CFRC printing and the obtained values are validated [11, 13, 15].

Table 1: Printing Parameter Set

<i>Printing Parameter</i>	<i>Value</i>
Wall Thickness	2.6 mm
Layer Height	1 mm
Overlap Factor	0.3
Nozzle Temperature	200°C
Heatbed Temperature	60°C
Printing Speed	50 mm/min

2.3. Materials

Co-axial carbon fibers are fibers with continuous reinforcement aligned along the filament's axis. As proven in the previous studies, co-axial printing with carbon-fiber enables improved mechanical and multifunctional properties [15]. In this study, the carbon-fiber filament is embedded within a thermoplastic matrix (PLA/TPU), enabling both structural reinforcement and thermal responsiveness. Markforged Carbon Fiber CFF filament was selected as the reinforcement material, while eSun 1.75mm PLA+ filament, pure PLA and custom-produced PLA/TPU mixture filaments were chosen for the matrix. These materials were selected for their complementary properties, which improve both the mechanical and functional performance of the resulting composite. Pure PLA, PLA+ and PLA/TPU mixtures can facilitate smart material behavior in structures for various applications. Combining these materials in different compositions broadens the range of functionalities that smart materials can offer. The matrix material, PLA (Polylactic Acid), is a widely used biodegradable polymer known for its ease of use in 3D printing and environmental sustainability. When PLA is reinforced with carbon fibers, its mechanical properties, such as compression and tensile strength, along with modulus, are significantly improved, creating a composite with superior energy absorption capabilities. PLA+ is recognized for its increased strength and ductility compared to pure PLA. To validate these enhanced properties, a well-known shell product is used for comparison. TPU, known for its flexibility, is especially advantageous in applications involving cyclic loading. To assess various PLA/TPU mixture combinations, several filaments were produced with the assistance of a local custom filament supplier. Five different combinations (ranging from 10% to 50% TPU) were used to produce filaments.

The production of PLA/TPU filaments is carried out by a local custom filament manufacturer as mentioned above. The process starts with raw material preparation for extrusion and final filament formation. Initially, PLA and TPU powders with varying TPU ratios (10%, 20%, 30%, 40%, 50%) are dried to remove residual moisture. Proper drying ensures consistent melt flow behavior and prevents defects in filament. Once dried, the polymer blends are processed using a twin-screw extruder, which facilitates uniform mixing and dispersion of

TPU within the PLA matrix. The extrusion process follows a controlled temperature profile, with heating zones set at 60°C, 140°C, 180°C, 190°C, and 200°C for 5 different blends, which satisfies effective blending. The extrusion was performed at a screw speed of 200 rpm, which provides sufficient shear force to homogenize the polymer.

Previous studies highlighted the effects of different PLA-TPU concentrations in terms mechanical properties under compressive and tensile loads [11, 31]. These studies showed that changing the ratio of PLA-TPU in the matrix, directly effecting the material properties such as energy absorption capacity, shape recovery etc. Also, they suggested that increasing the TPU content by more than 50% causes manufacturing problems during filament production and printing. Characterization of PLA/TPU filaments (*Section 4.1*) made with DMA and DSC tests to obtain material properties, essentially glass transition temperature (T_g).

2.4. Energy Absorption and Reusability Evaluation of CFRCs

One of the main applications for smart CFRC structures is reusable energy absorption. To assess their energy absorption capabilities, quasi-static uniaxial compression tests were performed using a ZwickRoell Universal Testing Machine (UTM) at room temperature, with a constant crosshead speed of 5 mm/min. The force-displacement curves obtained from these tests were analyzed to evaluate the energy absorption behavior of the samples. As shown in *Figure 6*, the force-displacement curve typically follows three stages. Initially, force increases linearly as deformation occurs until micro-buckling or cracking begins within the structure. This is followed by a plateau region where the force remains nearly constant over a range of deformation, up until the onset of densification, labeled as δ_d . Beyond δ_d , the structure enters the densification phase, where the force increases rapidly with further displacement.

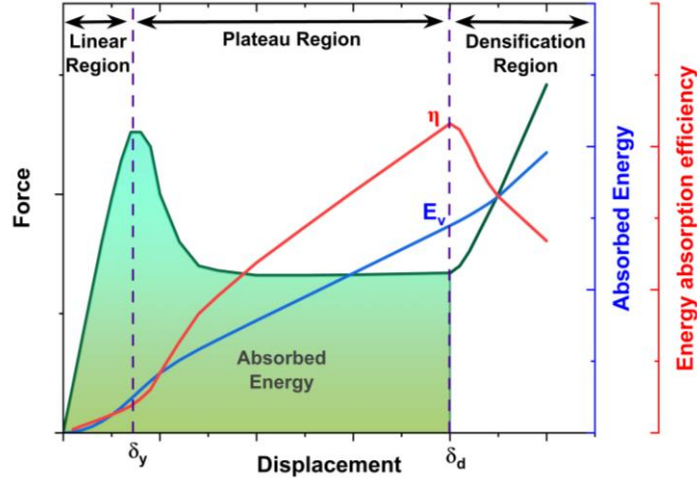


Figure 6: Force-Displacement curve for energy absorption calculations

To quantify the energy absorption properties, several metrics were applied for auxetic unit cell and hexagonal cellular CFRCs. The absorbed energy, E_v (Eq.1), was determined as the area under the force-displacement curve up to the densification point δ_d using the following equation [32, 33]:

$$E_v = \int_0^{\delta_d} F(\delta) d\delta \quad (1)$$

The specific energy absorption, which measures the absorbed energy per unit mass, is computed by dividing the volumetric energy E_v by the material mass m . [35, 44].

$$SEA = \frac{\int_0^{d_{max}} F dl}{m} = \frac{E_v}{m} \quad (2) \quad MCL = \frac{\int_0^{d_{max}} F dl}{d_{max}} \quad (3) \quad CLE = \frac{MCL}{IPCF} \quad (4)$$

Mean Crush Load (MCL) represents the average load sustained by a sample over the maximum displacement during deformation. It reflects the material's overall load-bearing capacity. Critical Load Efficiency (CLE) evaluates the relationship between the material's Mean Crush Load and its Initial Peak Crushing Force (IPCF) and it gives clues about stiffness after reaching peak force value [44-46]. For the structures with fewer force resistance decrease after yielding point this value will be close to 1

The energy absorption efficiency, η (Eq.5), was also calculated for auxetic unit cell to evaluate how efficiently the structure absorbs energy at each displacement increment [34]. The following formula was employed, where the initial length of the sample (L) was included in the denominator to normalize the efficiency [45, 46]:

$$\eta(\delta_i) = \frac{\int_0^{\delta_i} F(\delta) d\delta}{F(\delta_i).L} \quad (5)$$

Efficiency reaches its peak at the onset of densification, δ_d , after which energy absorption becomes less effective. The energy absorption efficiency was used to determine the optimal material composition and assess the impact of reinforcement across various mixtures.

To quantify the reusability of the auxetic unit cells, two metric termed Reusability Factor 1 (R_{RF1}) and Reusability Factor 2 (R_{RF2}) are introduced where $(E_v)_{C_i}$ represents the energy absorption of the structure during the i^{th} cycle of the compression test. Based on this terminology, if the structure can absorb the same amount of energy in the i^{th} cycle as it did in the first cycle, the Reusability Factor 1, $R_{RF1}=1$, indicating that the structure energy absorption properties is equal to initial cycle. Similar to that if the structure can absorb the same amount of energy in the $(i + 1)^{\text{th}}$ cycle as it did in the i^{th} cycle, the reusability factor $R_{RF2}=1$, indicating that the structure energy absorption properties is equal to previous cycle. Conversely, if $R_{RF1}<1$ or $R_{RF2}<1$, it suggests a decline in energy absorption, while structures with higher R_{RF1} and R_{RF2} values are more desirable in terms of reusability. Since different applications may need different requirements in terms of reusability, it is logical to use two separate terms while evaluating reusability capabilities. R_{RF1} indicates how energy absorption changes relative to the first cycle, while R_{RF2} reflects changes compared to the preceding cycle.

$$R_{RF1} = \frac{(E_v)_{C_i}}{(E_v)_{C_1}} \quad (6) \quad R_{RF2} = \frac{(E_v)_{C_{i+1}}}{(E_v)_{C_i}} \quad (7)$$

During this study, the fabricated CFRC structures are evaluated respect to presented energy absorption formulations. This evaluation first starts with effects of different path planning

approaches on energy absorption. Then different material combinations are examined for CFRC structures and energy absorption-reusability investigation proceeded. Finally, effects of different cellular structure geometries are evaluated in terms of energy absorption.

2.5. Cold programming of CFRCs

The cold programming cycle of CFRCs involves two stages: programming and recovery. In the programming stage, the material is deformed from its original shape into a new, temporary shape. During the recovery stage, CFRC can revert to their original shape when exposed to a heat. This shape recovery feature of CFRC differs from the elastic recovery seen in hyper-elastic materials like rubber. The cold programming ability is one of the key features that makes CFRCs, smart material. The cold programming procedure is illustrated in *Figure 7*. Before programming under compression, the initial dimension of each sample, L_1 , was measured. The sample was then deformed under load until it reached the specified deformation, L_2 . Upon unloading, the sample recovered part of its previous deformation, and its dimension became L_3 , which was considered the programmed shape. After heating the deformed samples above the polymer's T_g temperature, the final dimensions were measured and labeled as L_4 which represents recovered length.

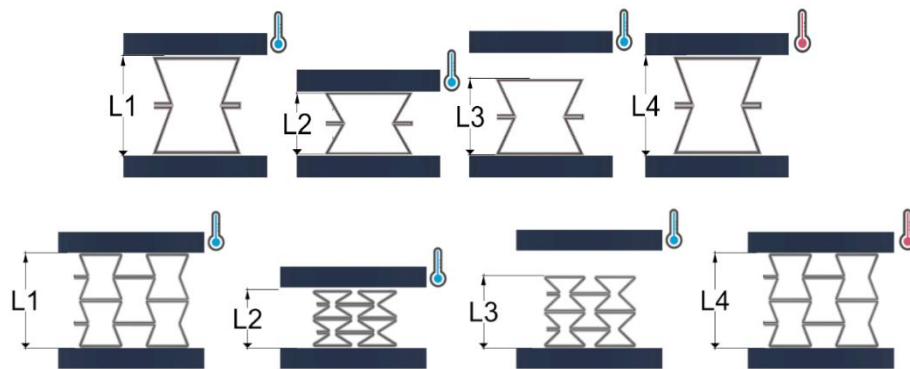


Figure 7: Cold programming cycles of auxetic unit cell and cellular structure

2.6. Shape Recovery and Shape Fixity Evaluation of CFRCs

Cyclic shape memory characteristics of CFRCs are measured using the shape recovery ratio (R_{r_i} – Eq. 9) and shape fixity ratio (R_{f_i} – Eq. 8). Ideally, $R_{r_i} = R_{f_i} = 1$, indicating the structure perfectly retains its temporary shape and fully recovers its original form during the recovery process. However, in practice, these values typically show ratios less than one, reflecting slight variations in shape fixity or recovery performance.

$$R_{f_i} = \frac{L_{1i} - L_{3i}}{L_{1i} - L_{2i}} \quad (8)$$

$$R_{r_i} = \frac{L_{4i} - L_{2i}}{L_{1i} - L_{2i}} \quad (9)$$

Two primary techniques are commonly employed to initiate the shape recovery process in smart materials: hot-water heating and Joule heating. Hot-water heating is a widely used method, where the deformed structure's temporary shape is erased, and the original shape is restored by immersing the material in hot water, utilizing the thermomechanical properties of the polymers involved. Joule heating, on the other hand, generates heat within the material by applying an electric current through a conductive pathway. This approach has been utilized in 4D printing to selectively or cumulatively heat specific areas, triggering controlled shape transformation.

In CFRC structures, carbon fibers contribute dual functionality: enhancing the mechanical strength of the composite and acting as conductive pathways for Joule heating. Researchers have demonstrated the effectiveness of incorporating conductive elements like carbon nanotubes or metallic nanoparticles into 3D-printed polymers to achieve precise control over shape transformation. By integrating carbon fibers into the CFRC matrix, a conductive network can be established, allowing Joule heating to serve as a uniform and controlled heat source [36, 47-50]. This facilitates precise and localized heating, enabling accurate and predictable shape recovery processes. Additionally, embedding electrical circuitry into carbon fiber reinforcements streamlines the manufacturing process and allows for the development of smart, electro-active materials with programmable shape-changing capabilities. Incorporating electro-active components within the metamaterial matrix creates materials that respond adaptively to external stimuli, paving the way for advanced,

responsive material systems [12, 49, 51]. To implement Joule heating, layers of printed parts are used as parallel resistors. Those resistors are enabled heating the structure. Via connection points, structures are connected to power supply. In the scope of this research, parts are fabricated with 8 layers. And every part is formed with two parallel current loops. A representation of these two methods could be seen on *Figure 8*.

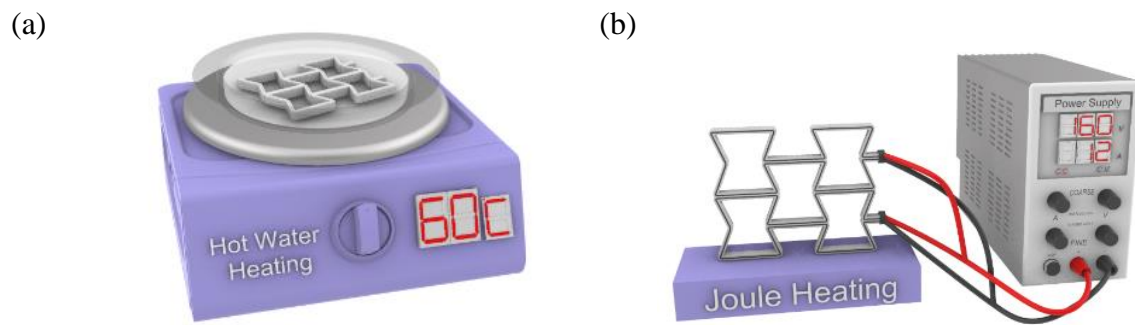


Figure 8: Illustrations of recovery methods: (a) Hot water recovery, (b) Joule heating

3. CONTINUOUS PATH PLANNING OF CFRCs AND FABRICATION

3.1. Continuous Path Planning of Hexagonal Cellular CFRCs

The manufacturing of Carbon Fiber Reinforced Composites (CFRCs) requires a continuous printing process because the fiber cannot be cut during printing without any specialized equipment. Extrusion based additive manufacturing processes pose specific challenges due to the need for frequent starts and stops in the extrusion process, which can lead to material inconsistencies. Additionally, idle movements across the printing bed can cause the carbon fiber to be pulled and result with a failed part. Therefore, specialized continuous path planning algorithms are essential.

For cellular CFRCs, a novel procedural path planning algorithm was developed due to the grid-like structure and repetitive patterns. This algorithm allows for the parametric design of samples with varying hexagonal cellular configurations. The resulting path forms a network of interconnected points, ensuring an uninterrupted trajectory throughout the structure. The dimensional inputs and parameters are processed to create printing instructions for the printer. Pseudo-code of the cellular path planning presented in *Algorithm 1*. In this code, unit cell edge length (L_{edge}), number of cells in each row (n_{row}), number of cells in each column (n_{column}) and cell inner angle (A) are defined as inputs to parametrize cellular structure. The code uses these parameters to calculate point locations sequentially. This algorithm creates hexagonal cell units. This algorithm could be further refined for other types of structures. To

create hexagonal cellular structures, nested for loops defined to proceed a routine. This routine uses cosine-sine of inner angle (A) and calculates printing path points (T_{Gcode}).

Algorithm 1 Hexagonal Cellular Structure Generation Algorithm

INPUT: L_{edge} , n_{row} , n_{column} , A

OUTPUT: $\{T_{Gcode}\}_{c=0,\dots,C}$

START

1. $c \leftarrow 0$; $T_{Gcode} \leftarrow \{\}$
2. **For** (i = 0 to n_{row} step 1) {
3. **For** (j = 0 to n_{column} step 1) {
4. $P_1 = (x - L * \sin(A), y + L * \cos(A))$
5. $P_2 = (x, y + L)$
6. $P_3 = (x + L * \sin(A), y + L * \cos(A))$
7. $P_4 = (x, y - L)$
8. $T_{Gcode}(c; c+1; c+2; c+3) = P_1; P_2; P_3; P_4;$
9. $c = c + 1$ }
10. **For** (j = 0 to n_{column} step 1) {
11. $P_1 = (x + L * \sin(A), y - L * \cos(A))$
12. $P_2 = (x, y - L)$
13. $P_3 = (x - L * \sin(A), y - L * \cos(A))$
14. $P_4 = (x, y + L)$
15. $T_{Gcode}(c; c+1; c+2; c+3) = P_1; P_2; P_3; P_4;$
16. $c = c + 1$ }
17. }

END

This pseudo-code is implemented on Rhinoceros3D with Rhino Script add-in. This pseudo code outlines the process of generating a hexagonal grid using a series of directional movements based on specified parameters. The code iterates through rows and columns to draw a series of points, simulating the structure of a hexagonal pattern. For each row and column, the code calculates path points and repeats this pattern. The point declaration in each step is calculated by adjusting the x, y, and z coordinates of the point using trigonometric formulas. By varying the input angle, the same algorithm can produce both honeycomb and auxetic structures, offering flexibility in structural design. Additionally, an overlap factor was integrated into the algorithm to manage the intersections of neighboring lines and regulate the penetration between printed lines. *Figure 9* presents several examples of the

Rhino Script applied with varying structural parameters edge length (L), inner angle (A), number of rows (η_r) and number of columns (η_c). As shown, it is possible to generate hexagonal structures with completely continuous, thanks to a passing line at the start and end of each column.

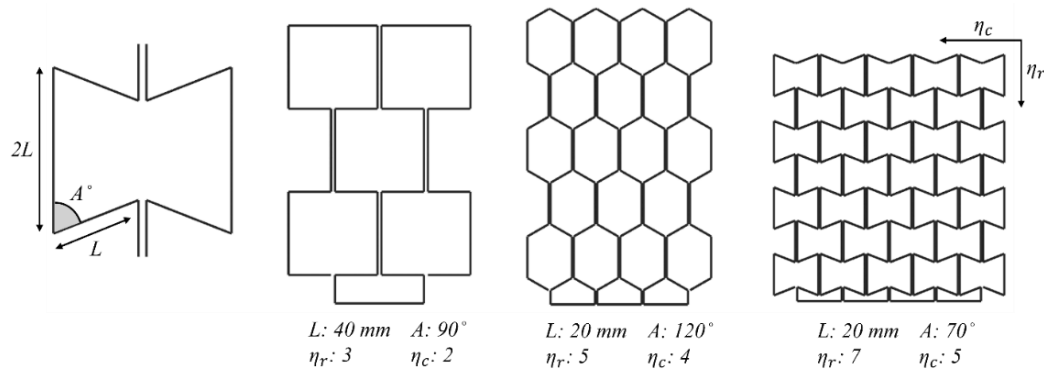


Figure 9: Hexagonal cellular paths with different parameters like edge length (L), inner angle (A), number of rows (η_r) and number of columns (η_c).

To evaluate cellular CFRC smart material properties, like compressive strength, flexural properties, and shape memory performance, an auxetic unit cell and three different cellular CFRC structures were prepared. The auxetic unit cell design proceeded to evaluate materials shape recovery properties. For different extrusion materials, unit cell design (*Figure 10*) is used and smart materials properties examined. Previous studies showed that, the unit cell design can be tiled and scaled up for larger components while retaining its mechanical properties and it is proven by computational simulations [52].

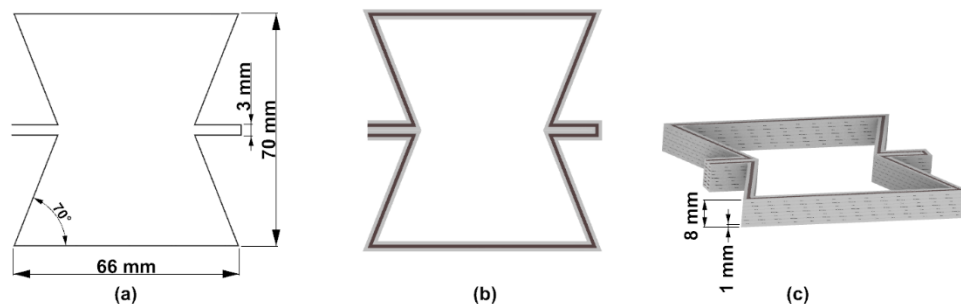


Figure 10: (a) Dimensions of the auxetic unit cell, (b) Top rendered view of the CFRC unit cell with carbon-fiber, (c) Layer height and total height of the CFRC unit cell design

A key application of smart materials is energy absorbers. To assess their energy absorption capabilities, an auxetic re-entrant structure, a honeycomb structure, and a brick structure were designed using *Algorithm 1*. The salient angle (180° - inner angle) parameter is used and 70° , 90° , 110° are selected to evaluate structures. Besides that, all parameters like unit cell count, layer count, sample outer dimensions and printing parameters kept constant. At the testing phase those samples were named as D70, D90, D110. The designed sample part dimensions and rendered views could be seen on *Figure 11*.

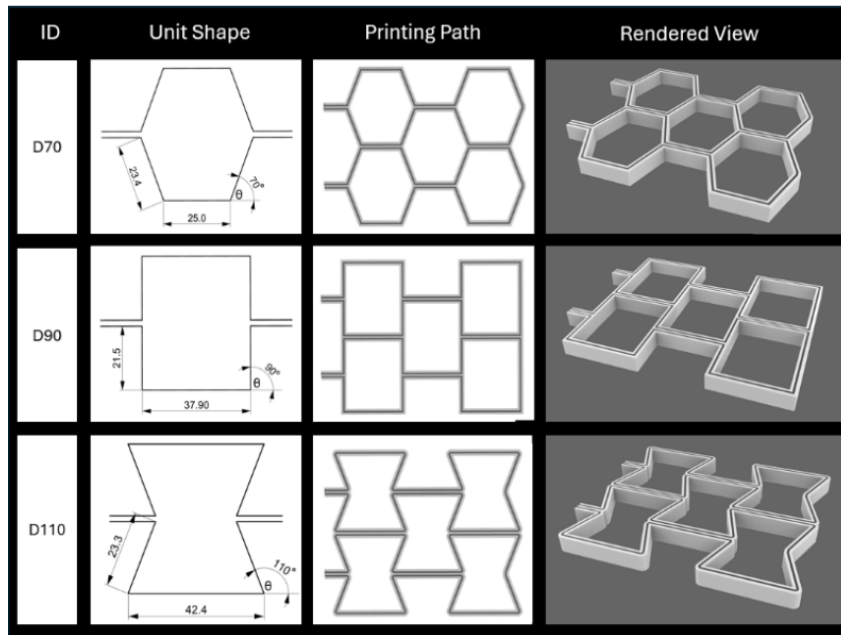


Figure 11: D70, D90, D110 CFRC sample part designs

The designed samples are fabricated with materials which discussed in *Section 2.3*. To evaluate the effects of carbon-fiber reinforcement, designs fabricated with and without carbon-fiber reinforcement. During printing, local breakages of the carbon fibers were observed due to inconsistencies in the flow of the melted material. However, in general, the fibers aligned with the printing path. It was also noted that the carbon fibers were slightly pulled at the sharp edges of the structure. Despite these issues, the part qualities and dimensional accuracy were satisfactory.

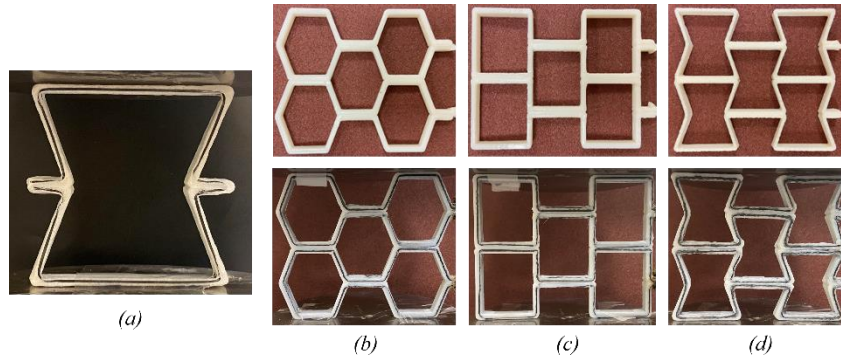


Figure 12: Fabricate auxetic unit cell (a), D70 (b), D90 (c) and D110 (d) sample parts

The generated continuous paths tend to be weaker at the intersections of rows when completing a full turn within the grid. To address this issue, three path planning approaches were evaluated: a conventional path, a path with intersecting crosslines, and a more intricate path which denoted as modified path. These variations aim to enhance uniformity and minimize anisotropy throughout the structure. Printing paths and the fabricated samples could be seen in *Figure 13*.

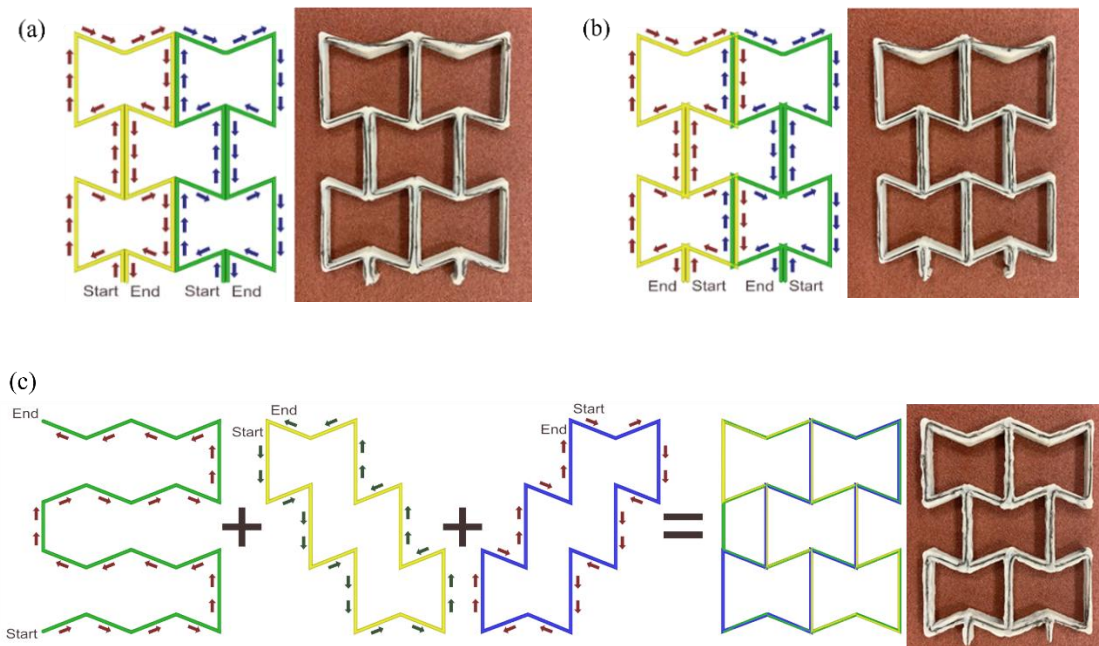


Figure 13: a) Conventional path, b) Crossed path, c) Modified path

The conventional path (a) and the crossed path (b) simply arranged with the help of overlap factor parameter and desired penetration obtained. For the modified path (c), path planning

completed in three steps and semi-continuous path generated. Since in the large scale discussed paths will be continuous generally, minor discontinuities neglected.

After that, compression tests were used to analyze mechanical properties of CFRCs which fabricated with the discussed path planning approaches. The tests are carried out on ZwickRoell-Universal Testing Machine with 100 kN compression grippers. For the tests, 1 mm/sec compression speed and %15 deformation ratio is selected. Initial, loaded and unloaded conditions of different paths could be seen in *Figure 14*. During compression tests, it is witnessed that the modified path showed a different deformation mode. Since the conventional and the crossed path deformed similar, the modified path deformed well settled and symmetric.

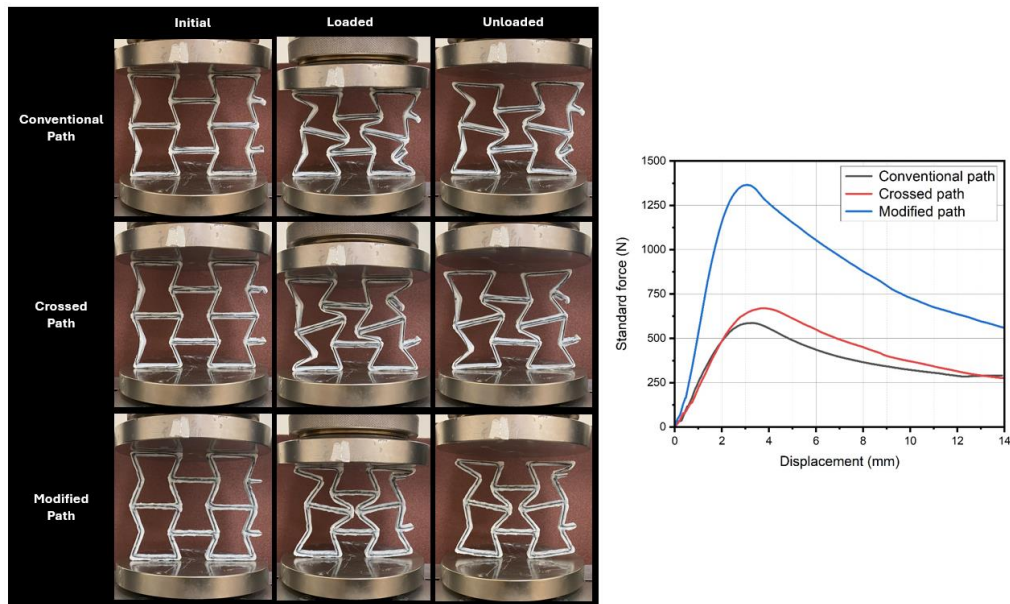


Figure 14: Compression test images and Force-Displacement curves of cellular auxetic CFRCs which printed with conventional, crossed and modified path

The compression test data is used to calculate the Initial Peak Crushing Force (IPCF), Specific Energy Absorption (SEA – *Eq.1*), Mean Crushing Load (MCL – *Eq.2*) and Crush Load Efficiency (CLE – *Eq.3*) parameters.

Table 2: Comparison of mechanical properties of different printing paths

<i>Printing Path</i>	<i>Mass(g)</i>	<i>IPCF(kN)</i>	<i>SEA(J)</i>	<i>MCL</i>	<i>CLE</i>
Conventional path	20.9	0.59	0.25	0.37	0.62
Crossed path	21.9	0.67	0.28	0.43	0.63
Modified path	29.87	1.36	0.41	0.86	0.63

Since the total printed mass will be different for different path planning approaches, these metrics are useful for comparing energy absorption smart material capabilities. *Table 2* presents the results for discussed path planning approaches. The sample with the modified path achieved a higher Mean Crush Load (MCL) of 0.86, demonstrating greater resistance to deformation compared to the conventional and crossed paths, which had MCL values of 0.37 and 0.43, respectively. However, Crush Load Efficiency (CLE) value stayed almost same for different paths which suggesting efficiency increase limited due to increase of mass. A more advanced algorithm is required to evaluate the energy absorption characteristics of solid, non-cellular geometries which is discussed in *Section 3.2*.

3.2. Continuous Path Planning of Solid CFRCs

Besides cellular CFRCs, printing paths of solid structure requires continuous hatch filling features. Since solid geometries could include features like holes or irregular border curves, it is essential to use a geometric based path planning algorithm to create hatch infill [13, 17, 18, 53]. The discussed cellular path planning algorithm creates path with a procedural grid generation approach to satisfy continuity. The proposed algorithm enables geometry-based path planning with geometric analysis of the input model. With geometry-based path planning, solid CFRCs with different requirements could be manufactured. The pseudo-code of the geometric based path planning algorithm is presented in *Algorithm 2*.

In this *Algorithm 2*, first the input model is divided into layers along the z-axis, allowing each layer to be filled independently. To perform slicing, the corner points of the bounding box enclosing the part are identified. This bounding box is generated based on the part geometry model, and its corner points are used to determine the minimum and maximum z-values. These values define the range of planes parallel to the xy-plane that slice the model into layers. Parameters such as nozzle diameter, overlap factor, and interlayer penetration factor are defined based on user input. The thickness of each layer is determined by the nozzle diameter and the interlayer penetration factor. The planes intersect the geometric model to generate closed contour curves for each layer, with the outer contours enclosing the inner ones. For each contour, the algorithm scans the contours to evaluate features and a raster scanning pattern is planned, where intersecting lines are generated along the y-axis within the bounding box at intervals determined by the nozzle diameter and overlap factor. During these processes, extremum points along the scanning direction are identified. With local minima and maxima points in the contour, the algorithm segments layer in printing regions. Identifying the maximum and minimum points is crucial to prevent unfilled areas and material deposition beyond the part during continuous filling [13].

Algorithm 2 Geometric-Based Continuous Path Planning Algorithm

INPUT: Model, d_{nozzle} , r_{overlap} **OUTPUT:** $\{T_{\text{Gcode}}\}_{c=0,\dots,C}$ **START**

1. $c \leftarrow 0$; $T_{\text{Gcode}} \leftarrow \{\}$
2. $B = \text{BoundingBox}(\text{Model})$
3. $n_{\text{layer_count}} = (B(z_{\text{max}}) - B(z_{\text{min}})) / d_{\text{nozzle}}$
4. **For** ($i = 0$ to $n_{\text{layer_count}}$ step 1) {
5. $\text{Plane}^i = z_{\text{min}} + i * d_{\text{nozzle}}$
6. $c^i = \text{Intersect}(\text{Model}, \text{Plane}^i)$
7. **For** (contour in c^i) {
8. $B_c = \text{BoundingBox}(\text{contour})$
9. $d_{\text{line_width}} = d_{\text{nozzle}} * (1 - r_{\text{overlap}})$
10. **For** ($j = 0$ to $\max(B_c)$ step $d_{\text{line_width}}$) {
11. $\text{Scan_line} = \text{Line}(\text{contour}, j * d_{\text{line_width}})$
12. $c^j = \text{Intersect}(\text{Scan_line}, \text{contour})$
13. **For** (point in c^j) {
14. $T_{\text{Gcode}}(c) = \text{point}$
18. $c = c + 1$ }
19. }
20. }

END

These points are determined by calculating the derivative of the curve along the scanning direction. After that, the algorithm implements a straightforward zig-zag path planning approach to hatch fill these regions with ensuring continuous path generation between regions. The zigzag pattern is designed to fully cover each layer with consistent material deposition and fiber orientation. The continuous path generated by the algorithm ensures that the fiber remains intact throughout the entirety of the printed structure, avoiding any potential weak points caused by discontinuities. Some generated continuous paths with geometric-based path planning approach could be seen in *Figure 15*.

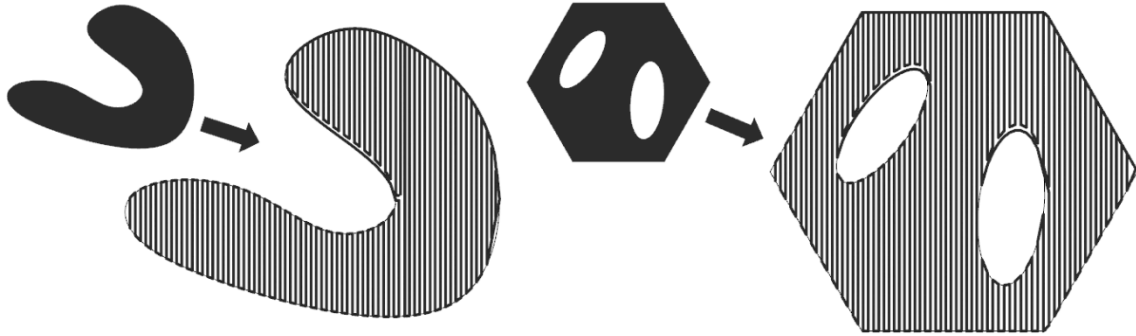


Figure 15: Example implementations of Algorithm 2

For CFRC structures, continuous path planning plays a crucial role due to the anisotropic nature of the material. CFRC structures are highly directional, meaning their mechanical properties vary depending on the placement of the fibers. This introduces an additional layer of complexity when designing load-bearing components with holes. To evaluate different continuous path planning approaches, plate with hole problem examined and effects of these approaches on mechanical properties are inspected and additional functionalities like hole reinforcement with spiral printing utilized. The plate with hole problem is a well-known challenge in structural mechanics and materials engineering. It involves studying how a hole or discontinuity within a plate affects its mechanical behavior, particularly under stress. Such structures are commonly found in real-world applications such as aerospace components, mechanical connectors, and pressure vessels, where material optimization is critical to ensure structural integrity [54-56]. An illustration from previous research about stress concentration of plate with hole could be seen in *Figure 16* [57].

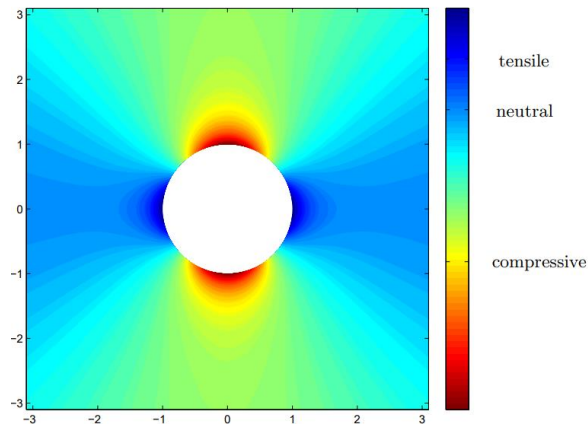


Figure 16: Stress concentration around plate with hole subjected to uniform tensile forces [57].

The primary concern is the high-stress concentration that occurs around the hole, leading to potential failure. In a typical plate without a hole, stress is evenly distributed throughout the structure. However, the presence of a hole creates localized stress concentrations, particularly at the edges of the hole. This behavior witnesses under tensile or compressive loads, where the hole acts as a weak point. Theoretical studies, including those based on elasticity theory and stress analysis, have shown that the maximum stress at the edge of the hole can be several times greater than the nominal stress applied to the plate.

For load bearing CFRC applications, even minor adjustments to the continuous path planning strategy can greatly enhance mechanical performance. To demonstrate this concept, three distinct path planning approaches (Path 1, Path 2, and Path 3) were introduced. In the first approach (Path 1), a solid plate structure was fabricated and later drilled to create a hole using a vertical drill. While this method is not ideal due to the additional processing required, it serves as a benchmark for comparison. The second approach (Path 2) utilized the Geometric-Based Continuous Path Planning Algorithm (*Alg. 2*) to directly fabricate a plate with a hole. Finally, the third approach (Path 3) incorporated a spiral path planning feature into the second approach to enhance the design. This optimization reinforced the hole's border with a spiral trajectory, improving the structural integrity of the CFRC component. When employing spiral trajectories, a new parameter, the number of spiral revolutions (η_{sr}). This parameter plays a critical role in adjusting the mechanical properties for various applications. The number of revolutions directly affects the alignment of carbon fibers along the load direction. If the number of revolutions is too high, the fiber density in the load direction decreases, leading to reduced reinforcement. Conversely, if the revolutions are too few, the reinforcement along the hole's trajectory becomes insufficient, resulting in a weaker plate with a hole. Thus, careful optimization of η_{sr} is essential to achieve balanced and effective structural performance. The discussed path planning approaches are illustrated in *Figure 17*.

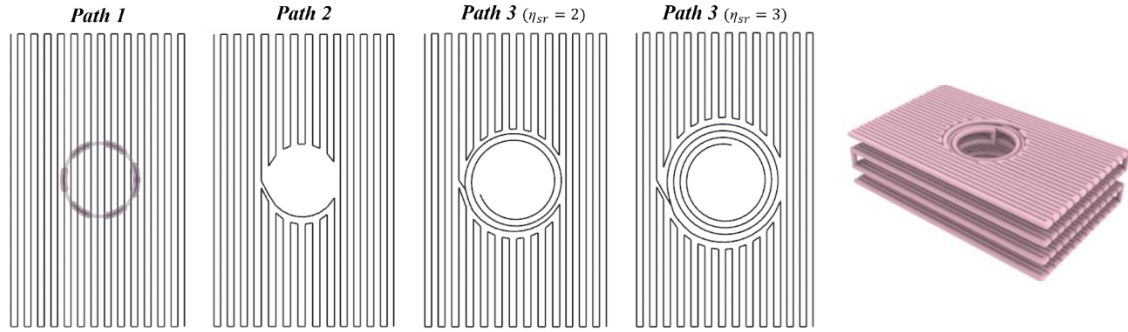


Figure 17: The proposed path planning approaches for plate with hole problem

Tensile tests were conducted on both unreinforced and reinforced (CFRC) structures. The tests were performed using a ZwickRoell Universal Testing Machine (UTM) at room temperature, with a constant crosshead speed of 5 mm/min. The initial and after-test conditions of tested specimens and force-strain plot could be seen in *Figure 18*. The multi-layered analysis was conducted to understand interlayer bonding and stress transfer around hole trajectory. The results showed that layering with spiral trajectory significantly improves load distribution around the hole.

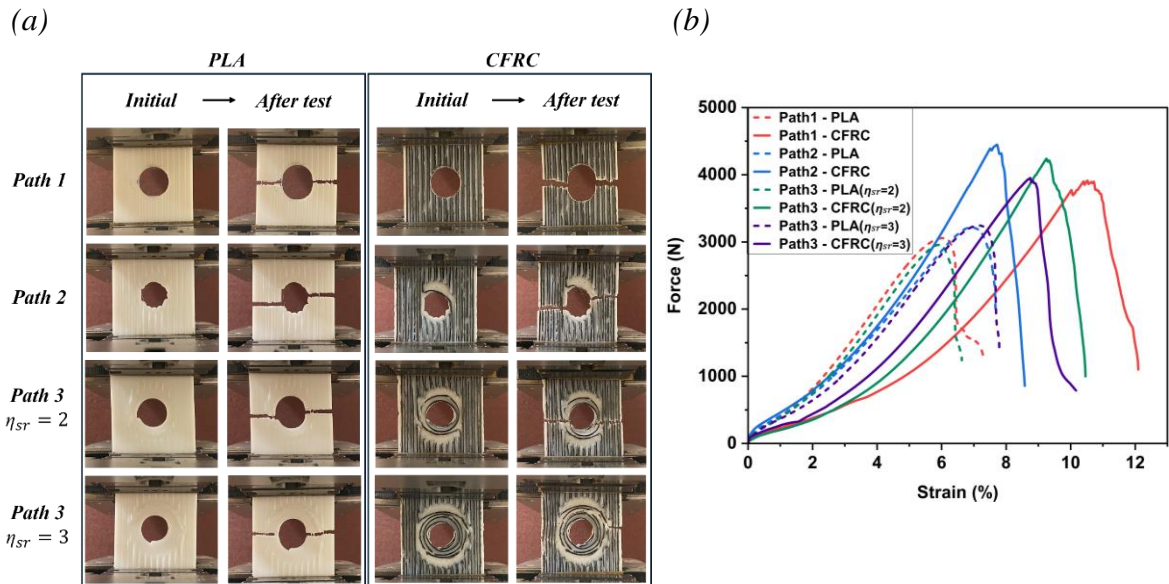


Figure 18: (a) Tensile test for PLA and CFRC structures, (b) Force(N)-Strain(%) plot of different path planning approaches

The tensile tests revealed that CFRC structures exhibited superior mechanical properties, as anticipated. While the unreinforced specimens (PLA) withstood tensile forces up to 3 kN, the CFRC samples demonstrated a higher ductility, reaching values between 4 and 4.5 kN.

The comparison of different path planning approaches revealed that Path 2 achieved the highest force value, attributed to the increased fiber count aligned with the load direction. However, it exhibited lower strain capacity, failing at 7.5% strain. Paths incorporating the spiral trajectory feature (Path 3) demonstrated improved strain performance, ranging between 8.5% and 9.5%. Among all methods, Path 1 showed the highest strain value due to its superior structural uniformity. Nevertheless, because of the additional post-fabrication processing required, Path 1 is considered as a non-practical approach. When evaluating the impact of different spiral revolution counts (η_{sr}), it was observed that Path 3 with $\eta_{sr} = 3$ exhibited inferior mechanical performance compared to with $\eta_{sr} = 2$. This outcome confirms that the spiral revolution count directly influences the fiber alignment along the load direction, as previously discussed.

4. COLD PROGRAMMING OF UNIT CELL PLA/TPU CFRCs

4.1. PLA/TPU Filament Material Characterization

To gain deeper insight into the properties of pure PLA and PLA/TPU mixtures, Differential Scanning Calorimetry (DSC) was used to evaluate thermal behaviors of the materials. This analysis provides valuable information about the material's crystallinity and heat response, which are critical for understanding its shape memory characteristics. The shape memory characteristics demonstrate the potential of these materials for use in smart applications, and the DSC results emphasize one of the key parameters of smart materials, the glass transition temperature (T_g). This transition point is particularly important for shape memory smart material applications, as it defines the temperature range where the material becomes flexible enough to be reshaped and subsequently returns to its original form upon reheating. The DSC analyses were conducted using a TA Q2000 instrument, calibrated with an indium standard and featuring Tzero functionality. All measurements were performed in a nitrogen atmosphere, with temperatures ranging from -50°C to 180°C , at a heating and cooling rate of $10^{\circ}\text{C}/\text{min}$ [11, 12]. The samples, consisting of 10 mg of pure PLA, TPU, and granular PLA/TPU mixtures, were prepared following a standard protocol and encapsulated in a typical DSC pan before measurement. The DSC results could be seen in *Figure 19*. It is witnessed that the pure PLA exhibits low crystallinity and typical semicrystalline behavior, while TPU shows a curve like an amorphous material. Unlike PLA, which crystallizes under specific conditions, TPU remains largely disordered, contributing to its amorphous behavior. TPU exhibits amorphous behavior due to lacking crystalline phase. The separation between hard and soft segments of the crystalline structure can influence its semi-crystalline behavior, depending on composition and processing conditions. The analysis also determined the glass

transition temperature (T_g) of PLA to be 65.64°C. The data show that increasing the TPU content has an impact on the T_g , with a slight decrease to 65.49°C for the 50% PLA - 50% TPU mixture. This small change in T_g indicates that pure PLA and PLA/TPU mixtures are highly compatible, and structures made from these materials will exhibit shape memory behaviors within the specified temperature range.

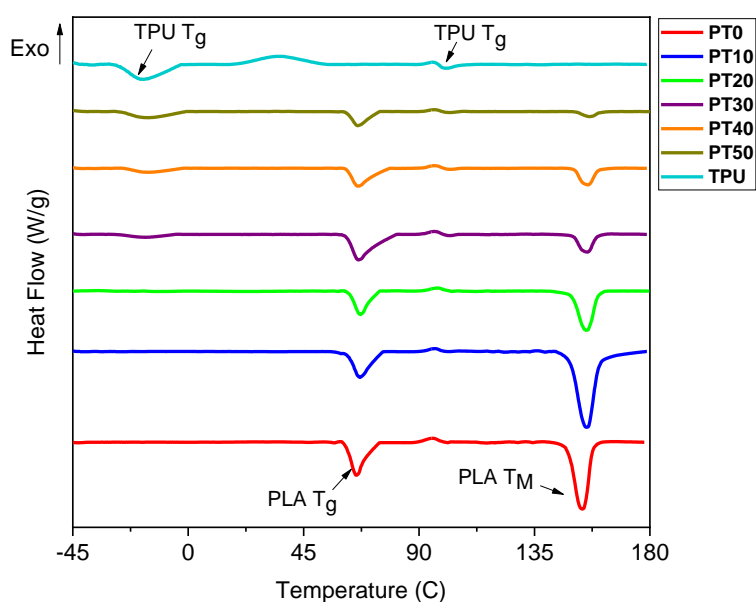


Figure 19: DSC results for pure PLA, TPU, and PLA/TPU mixtures

During DSC test, material's second heating cycle is used. Analyzing the second heating cycle in Differential Scanning Calorimetry (DSC) provides better insights about the material's thermal behavior. Because it eliminates the effects of previous thermal history, processing stresses, and residual stresses. Unlike the first heating cycle, which captures any physical aging, moisture evaporation, or recrystallization effects, the second heat data reflect the intrinsic thermal properties of the polymer blend.

One key parameter obtained from DSC is the change in heat capacity (ΔC_p) at T_g , which indicates the transition from the glassy to the rubbery state. A higher ΔC_p suggests greater molecular mobility and segmental motion in the amorphous phase, which can influence mechanical properties like toughness and shape recovery [11]. Additionally, the enthalpy change (ΔH), particularly during melting (ΔH_m) and crystallization (ΔH_c), provides information about the degree of crystallinity and thermal stability of the polymer blend.

These values are essential for evaluating how different polymer compositions interact and affect phase behavior.

Another effective technique for studying the thermo-mechanical behavior of materials is Dynamic Mechanical Analysis (DMA). DMA assesses the materials' response to mechanical stress at different temperatures, offering a more detailed understanding of its behavior. The DMA analysis was carried out using a Netzsch DMA 242 C analyzer. During tests, samples with 10 mm length were used under tension deformation. The analysis took place over a temperature range of 25°C to 120°C, with a heating rate of 3°C/min, a frequency of 1 Hz, and an applied strain of 0.001 mm/mm. The DMA curves for the pure PLA and PLA/TPU mixtures, showing the dynamic storage modulus and loss factor ($\tan(\delta)$), are presented in *Figure 20*.

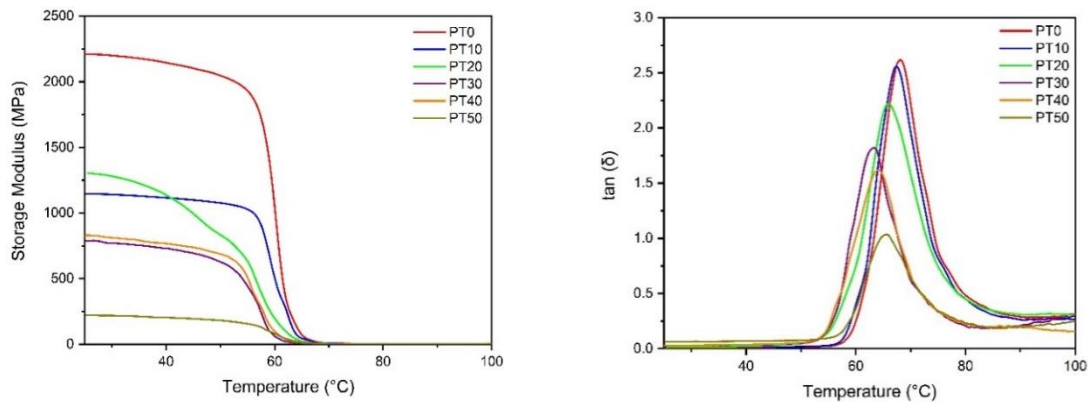


Figure 20: DMA results for pure PLA and PLA/TPU mixtures

The differences observed in DMA results are linked to shape recovery behavior. A higher storage modulus typically indicates better shape fixity, while a lower damping factor suggests more elastic recovery. The shape fixity and recovery properties of these materials will be investigated in *Section 4.4*.

These curves provide information about the materials stiffness and damping characteristics. One key observation is the sharp drop in the loss factor signaling the material's glass transition. The T_g measured in DMA is slightly higher than that observed in the DSC, which can be explained by the different measurement approaches: DMA evaluates the materials mechanical response, while DSC measures heat flow. Since the T_g of the mixtures can be determined by locating the temperature corresponding to the peak of the $\tan(\delta)$, the results

indicate that as the TPU content in the mixture increases, loss factor decreases as listed in *Table 3*. The analysis of pure PLA revealed that DMA and DSC techniques indicate different T_g values, which can be attributed to the distinct properties each method is sensitive to and accuracy of the test setup. The samples named respect to TPU ratio (ex. PT20 stands for 20% TPU)

Table 3: The T_g ($^{\circ}\text{C}$) of the PLA/TPU mixtures by DMA and DSC tests

<i>Sample</i>	<i>DMA</i>	<i>DSC</i>
PT0	68.12	65.64
PT10	67.28	66.88
PT20	65.93	67.64
PT30	63.23	66.48
PT40	64.15	66.04
PT50	65.3	65.49

The choice between Dynamic Mechanical Analysis (DMA) and Differential Scanning Calorimetry (DSC) for determining the glass transition temperature (T_g) depends on the nature of the material and the specific analysis requirements. DSC measures T_g by detecting changes in the heat capacity (ΔC_p) of the material as it undergoes a phase transition. This method is effective for identifying T_g in materials with distinct thermal transitions, such as amorphous polymers. However, DSC may not capture subtle transitions in complex polymer blends, especially if there is phase separation or overlapping transitions. DMA determines T_g based on changes in viscoelastic properties, particularly the storage modulus and $\tan \delta$ (damping factor). This method is more sensitive to mechanical transitions, making it ideal for detecting multiple T_g values in polymer blends or composites. Unlike DSC, DMA can measure the frequency-dependent nature of T_g , which is critical for understanding the behavior of polymers under loading conditions. For accurate correlation with shape recovery properties, DMA is preferred, as it better represents the functional performance of shape-memory polymers.

4.2. Cyclic Cold Programming of Unit Cell CFRCs

The cold programming behaviors and shape memory characteristics of CFRCs were investigated for various material compositions. Auxetic unit cells, as detailed in *Section 3.1.*, were fabricated using pure PLA and PLA/TPU blends. To enhance the brittleness and low toughness of PLA, TPU was incorporated into the blend. TPU and PLA are recognized for their biocompatibility, robust mechanical properties, and excellent shape memory performance, making them suitable for improving CFRCs in smart material applications [14–20]. Previous research has explored the shape memory properties of PLA/TPU blends extensively. For instance, Rahmatabadi et al. (2023) studied the performance of 3D-printed PLA/TPU structures (70/30 ratio) using PLA granules and polyester-based 90A TPU, analyzing the effect of printing parameters on shape memory behavior with the Box-Behnken design (BBD) [12, 38]. Similarly, Nejatpour et al. (2024) investigated the mechanical and shape memory characteristics of PLA/TPU blends prepared via high-speed thermo-kinetic mixing [11]. They identified blends with TPU content that offered mechanical properties comparable to pure PLA while maintaining sufficient flexibility at room temperature. Blends containing 20% TPU demonstrated optimal performance, including a high shape recovery ratio after significant deformation.

Building on these insights, PLA/TPU blends are used for 4D printing of CFRC auxetic structures for cold programming. Cold programming of the samples was conducted at room temperature, with deformation applied during compression tests considered the programming step. Cold programming applied with 30% and 50% deformation ratios, and it was based on the need to evaluate the material's mechanical response and shape recovery performance under moderate and severe deformation conditions. These values were chosen to reflect realistic strain levels that the material may experience in practical applications while ensuring that the deformation remains within the elastic and recoverable limits. 30% deformation represents a moderate strain level where the material undergoes significant but controlled deformation without excessive structural damage. This level is useful for assessing elastic recovery and minor permanent deformation effects. 50% deformation represents a higher

strain condition, approaching the material's limits. Testing at this level helps to evaluate the onset of plastic deformation, energy absorption behavior, and the material's ability to recover from more extreme conditions. Five programming and recovery cycles were performed. After five cycles of programming, the recovered samples could be seen in *Figure 21*. These sample parts are denoted as PT (PLA-TPU) and CPT (Carbon-fiber reinforced PLA-TPU) abbreviations with blend percentage information.

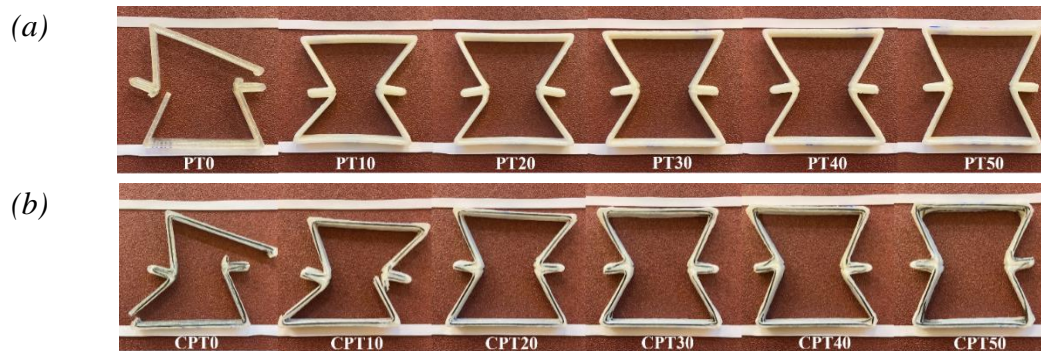


Figure 21: The recovered length comparison of PT (a) and CPT (b) samples after 5 cycles of programming-recovery

Figure 21 illustrates the recovered shapes of the samples after completing the fifth programming-recovery cycle, programmed with 50% deformation. The results clearly indicate that samples with higher TPU content exhibit improved shape recovery ability after repeated cycles. Most samples retained their shape memory properties after five cycles, apart from PT0, CPT0, and CPT10. These samples were unable to withstand 50% deformation and failed within a few cycles.

The initial, loaded, unloaded, and recovered states of the samples could be seen in *Figure 22*. *Figure 22a* shows the results of 30% deformation and *Figure 22b* **Figure 26** present for samples subjected to 50% deformation, respectively. Results showed that increasing TPU content improved elastic recovery after unloading. Following the recovery step, all samples nearly regained their original shape, highlighting the high potential of PLA/TPU blends for 4D-printed load-bearing structures. Auxetic behavior was evident as the structures exhibited inward shrinkage in the middle rather than outward expansion. Higher deformation levels led

to more pronounced permanent deformation across all samples. However, samples with higher TPU content (e.g., PT50, CPT50) demonstrated superior elastic recovery, while those with lower TPU content (e.g., PT10, CPT10) experienced greater plastic deformation and higher shape fixity ratios after unloading. This highlights that materials with lower TPU content are more prone to structural damage at higher deformations, whereas higher TPU ratios enhance resilience to large deformations with reduced residual strain.

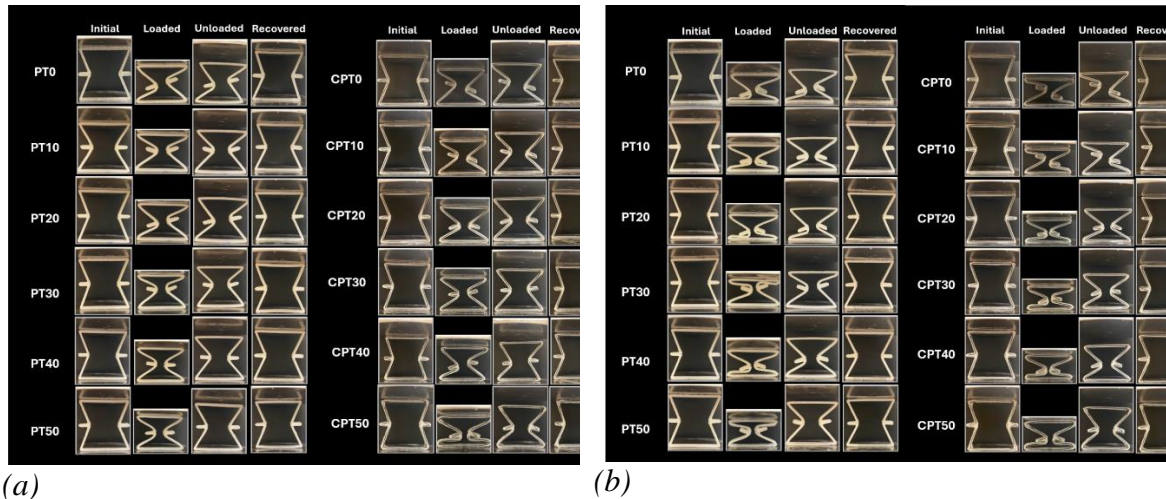


Figure 22: The cold programming of PT/CPT samples with 30% (a) and 50% (b) deformation

4.3. Energy Absorption and Reusability Investigation of CFRCs

Initially, the mechanical properties and energy absorption capabilities of auxetic unit cells made from PLA-TPU mixtures with different TPU percentages (0%, 10%, 20%, 30%, 40%, 50%) and with or without carbon-fiber reinforcement were evaluated. The mechanical behavior of these samples was tested under compression, with each sample undergoing five compression cycles. In *Figure 23* and *Figure 24*, the areas under the force-displacement curves represent the absorbed energy for each sample, with two deformation levels (30% and 50%) used to examine how deformation affects mechanical performance.

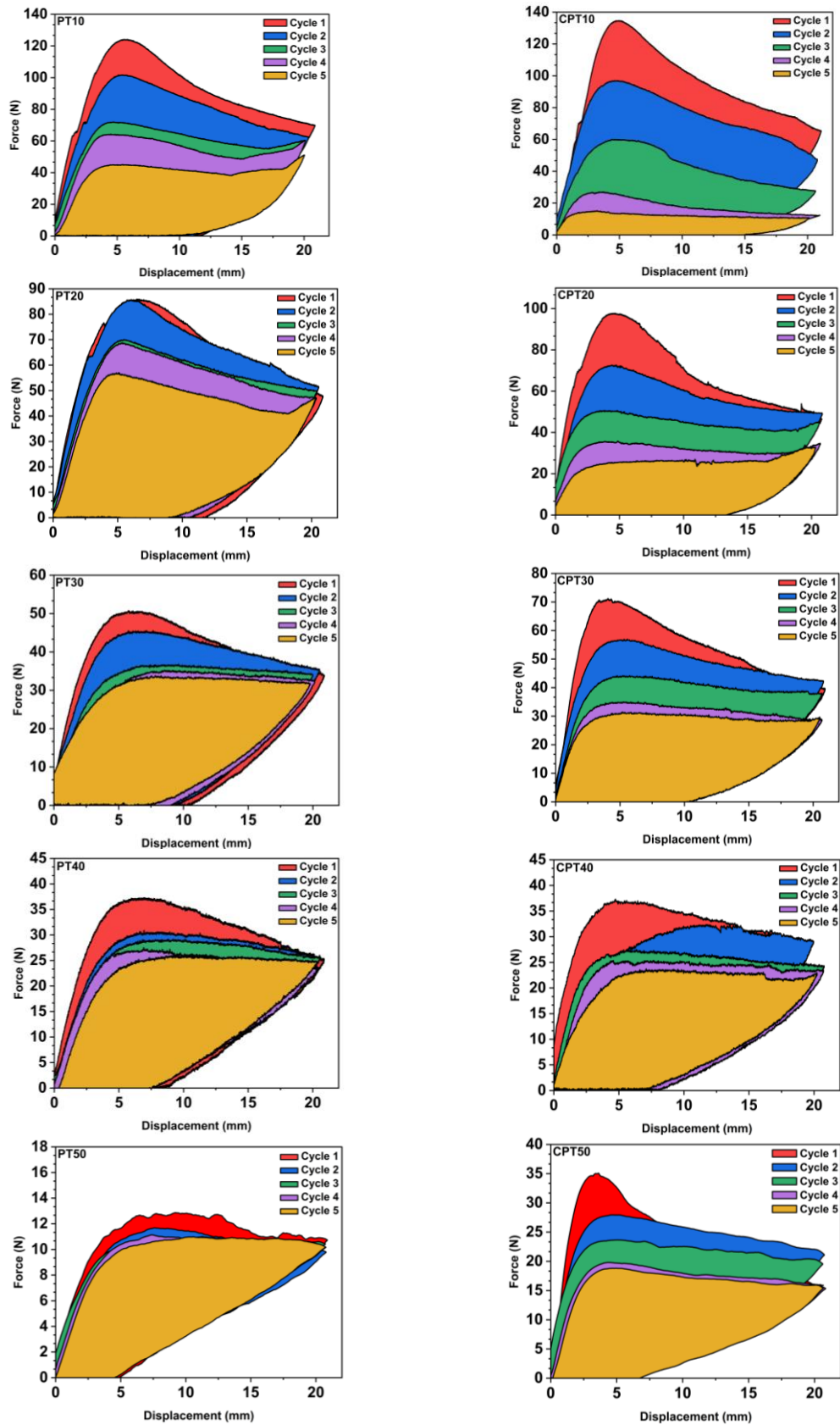


Figure 23: Force-displacement plots of PT and CPT samples under 30% deformation

As shown in *Figure 23*, the sample parts did not reach the densification point under 30% deformation. Samples with lower TPU content (PT10, CPT10, PT20, CPT20) exhibited high peak forces, indicating a stiffer structure. All sample parts maintained their structural integrity and underwent 5 cycles of programming without any breakage.

Another set of auxetic samples was tested with up to 50% deformation. The force-displacement curves of the PT and CPT auxetic structures, presented in *Figure 24*, show that structural failure was more likely at higher deformation, especially in samples with lower TPU content. The level of deformation applied had a significant impact on the mechanical response and energy absorption behavior of the samples. Notably, all samples subjected to 50% strain reached the densification region in their force-displacement curves, whereas no densification was observed in samples tested with only 30% strain. As a result, the structure remained largely intact for all TPU percentages at 30% deformation. However, at 50% deformation, structural failure occurred, with the CPT10 and PT10 samples breaking during the second and fourth loading cycles, respectively.

As previously mentioned, the primary reason for adding TPU to the material mixture was to improve the ductility of the 4D printed structure at room temperature. This enhancement was intended to make the materials suitable for compression, even under significant deformation, which is essential for load-bearing applications. Overall, the force-displacement graphs showed that adding TPU to the mixtures reduced the energy absorption differences between two successive cycles due to a softening effect. It was generally observed that the peak force significantly decreased between the first and second cycles, but in subsequent cycles, PT30, PT40, and PT50 exhibited similar force-displacement behaviors. The same behavior was observed in the CPT samples. Visual inspection of the force-displacement graphs revealed that increasing the TPU content in the mixtures reduced the softening effect, consistent with previous studies. Increasing the TPU content improves the suitability for compression but reduces the mechanical and energy absorption properties. Therefore, to achieve a reusable structure with adequate mechanical properties for load-bearing applications, it is crucial to determine an optimal balance between PLA and TPU content in the mixture.

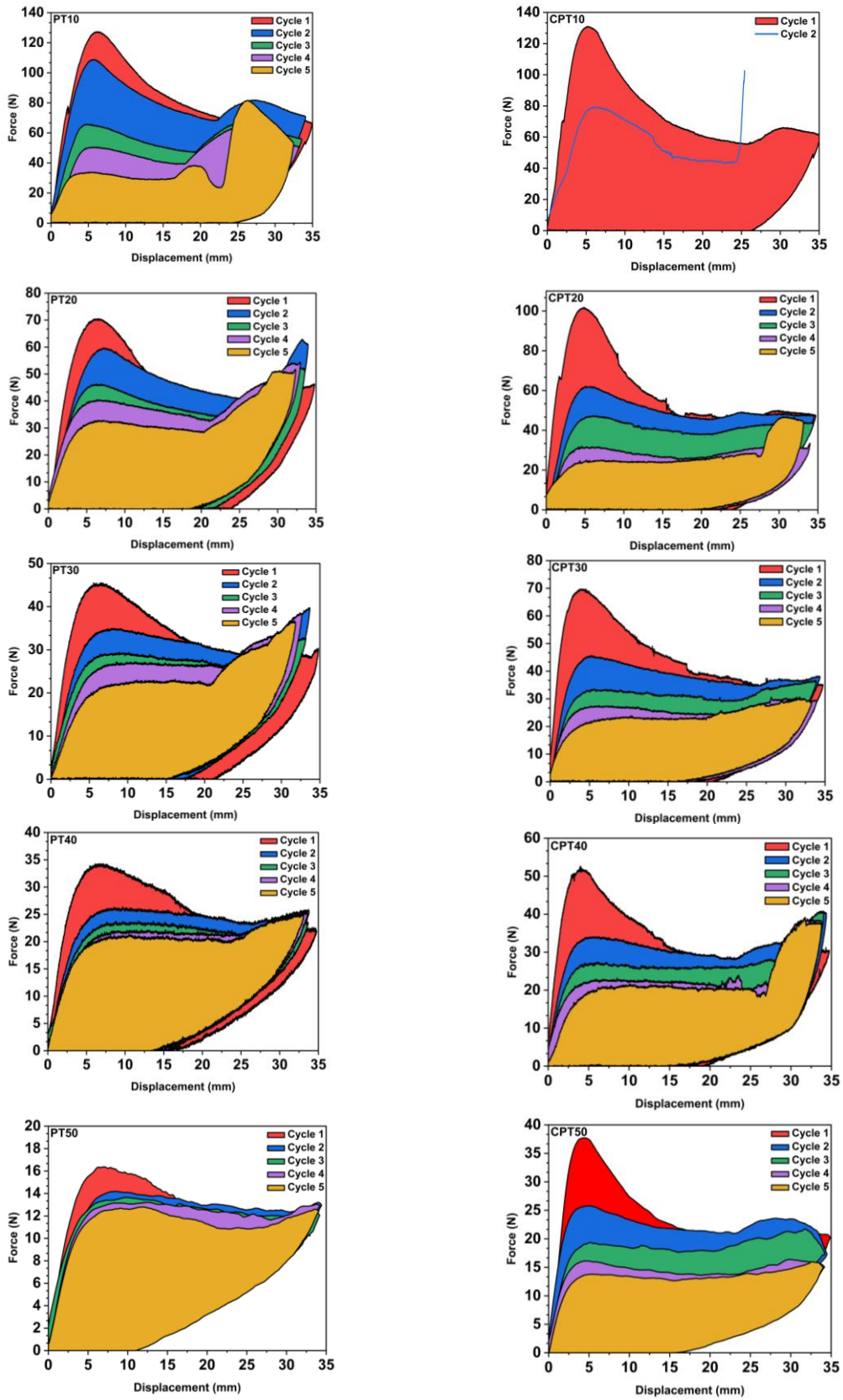


Figure 24: Force-displacement plots of PT and CPT samples under 50% deformation

Specifically, the densification points of the samples, total absorbed energy, and energy absorption efficiency were calculated and are presented in *Table 4*. The results clearly show that efficiency declines as the number of loading cycles increases for all cases.

Table 4. Energy absorption analysis of PT (unreinforced) samples under 50% deformation

<i>Sample</i>	<i>Cycle</i>	δ_a	E_v (mJ)	<i>IPCF</i> (N)	<i>SEA</i> (mJ)	η
PT10	1	27.32	2350	127.4	325.03	0.51
	2	22.43	1810	108.5	250.35	0.37
	3	19.55	1015	65.7	140.39	0.3
	4	17.97	723	50.55	100.00	0.26
	5	-	-	-	-	-
PT20	1	26.06	1238	70.35	197.13	0.52
	2	25.98	1180	59.57	187.90	0.41
	3	23.42	867	46.08	138.06	0.36
	4	21.49	739	40.12	117.68	0.32
	5	20.94	578	32.78	92.04	0.28
PT30	1	-	942	45.25	142.73	0.56
	2	26.54	797	34.77	120.76	0.39
	3	24.82	632	29.35	95.76	0.35
	4	23.29	554	26.92	83.94	0.29
	5	20.95	414	22.39	62.73	0.27
PT40	1	-	890	34.21	133.03	0.57
	2	-	788	26.16	117.79	0.44
	3	-	706	24.17	105.53	0.43
	4	-	669	25.27	100.00	0.39
	5	-	657	24.9	98.21	0.38
PT50	1	-	418	16.39	63.91	0.57
	2	-	416	14.28	63.61	0.5
	3	-	413	13.38	63.15	0.48
	4	-	393	12.98	60.09	0.44
	5	-	365	12.92	55.81	0.41

In samples with a low amount of TPU, the reduction in efficiency is more significant compared to samples with higher TPU content. For instance, for PT10, efficiency drops from 0.51 in the first cycle to 0.26 at fifth cycle (~51% reduction) while for PT50 the efficiency drops from 0.57 in the first cycle to 0.41 at fifth cycle (~30% reduction). This decline in efficiency aligns with a reduction in the structure's capacity to absorb energy and withstand

applied loads, as seen in the decreasing values of E_v and IPCF over time. It is worth noting that, despite the slight reduction in efficiency, samples with higher TPU content absorb less energy than those with lower TPU content. For example, E_v values for PT10 and PT50 in the first cycle are 2350 mJ and 418 mJ, respectively. This indicates that while these samples may absorb less energy, they maintain the ability to deform under load without reaching densification, reflecting a trade-off between energy absorption capacity and material durability.

Another significant effect of increasing TPU content is the delay in densification, even after significant deformation (e.g., 50%). As TPU content increases, densification occurs at higher deformation levels, and for PT40 and PT50, no densification was observed. It is well known that once densification occurs, the energy absorber is no longer useful, as force increases directly with applied deformation. The densification points were identified as the efficiency peaks. Moreover, results indicate that densification starts earlier in later cycles, likely due to residual damage within the structures, which allows them to deform more easily than in the initial loading cycles.

Table 5 displays the energy absorption characteristics of the reinforced samples. The results show that incorporating continuous carbon fiber substantially improves both the mechanical and energy absorption properties of all samples, compared to the unreinforced ones, highlighting the potential for enhancing the mechanical performance of 4D-printed structures for load-bearing applications

Table 5. Energy absorption analysis of CPT (reinforced) samples under 50% deformation

<i>Sample</i>	<i>Cycle</i>	δ_a	<i>EA(mJ)</i>	<i>IPCF(N)</i>	<i>SEA (mJ)</i>	η
CPT10	1	26.14	2071	130.58	273.22	0.53
	2	24.45	1337	79.1	176.39	0.43
	3	-	-	-	-	-
	4	-	-	-	-	-
	5	-	-	-	-	-
CPT20	1	-	2047	101.6	306.44	0.62
	2	-	1670	62.9	250.00	0.51
	3	-	1370	47.17	205.09	0.46
	4	33.52	937	31.48	140.27	0.43
	5	27.48	665	28.32	99.55	0.35
CPT30	1	-	1556	69.52	209.70	0.64
	2	-	1288	45.4	173.58	0.48
	3	-	1040	36.53	140.16	0.45
	4	-	854	29.77	115.09	0.41
	5	-	774	29.72	104.31	0.38
CPT40	1	-	1167	51.79	168.64	0.55
	2	31.18	940	33.97	135.84	0.43
	3	29.75	754	28.03	108.96	0.38
	4	27.23	574	23.67	82.95	0.37
	5	26.95	512	21.5	73.99	0.37
CPT50	1	-	414	16.62	60.61	0.57
	2	-	410	14.24	60.03	0.45
	3	-	403	13.67	59.00	0.45
	4	-	391	13.31	57.25	0.44
	5	-	366	12.95	53.59	0.41

Furthermore, carbon fiber reinforcement significantly influences the deformation behavior, delaying densification in the reinforced samples. For example, CPT20 exhibited a much higher resistance to early densification, retaining its mechanical properties over three cycles. The reinforcement allowed these samples to endure higher forces and maintain structural integrity over time. Samples like CPT30 and CPT50 were able to undergo five cycles without reaching densification. Although, similar to unreinforced samples, there was a reduction in energy absorption between cycles, the overall performance and efficiency stability of the CPT samples were superior to that of the PT samples.

The experiment is repeated two more times for PT10, PT20, PT30, CPT10, CPT20 and CPT30 samples. The standard deviation values for absorbed energy (E_v) and peak force (IPCF) are presented in *Table 6*. It is witnessed that generally the results deviate approximately 2-4% and reinforced samples showed lower deviation profile for IPCF values.

Table 6: Standard deviation values for PT10, PT20, PT30, CPT10, CPT20 and CPT30 samples

<i>Sample</i>	<i>Cycle</i>	σ_{E_v} (mJ)	σ_{IPCF} (N)
PT10	1	87.8	5.3
	2	43.1	3.9
	3	32.2	1.4
	4	46.2	2.9
	5	-	-
PT20	1	36.6	2.6
	2	39.4	2.4
	3	22.4	3.4
	4	19.3	3.9
	5	13.7	2.6
PT30	1	34.0	1.8
	2	32.7	2.4
	3	24.6	1.7
	4	22.6	1.2
	5	21.3	1.6
CPT10	1	102.5	6.4
	2	66.8	2.3
	3	-	-
	4	-	-
	5	-	-
CPT20	1	53.5	2.4
	2	49.7	1.4
	3	31.5	1.1
	4	26.5	2.7
	5	22.1	1.3
CPT30	1	26.5	1.8
	2	43.2	1.3
	3	24.8	1.4
	4	22.5	1.3
	5	26.9	1.8

Efficiency values are calculated using *Eq.7 (Section 2.4.)*, was used to compare the mechanical performance of the samples. In unreinforced samples, efficiency decreased sharply with each cycle. For instance, PT10 started with an efficiency of 0.54 in the first cycle, but this value dropped significantly due to the degradation of the material's mechanical properties, indicating a rapid loss of energy absorption under cyclical loading. In contrast, fiber-reinforced samples showed more consistent efficiency across cycles. CPT20, CPT30, CPT40, and CPT50 demonstrated a more gradual decline in efficiency compared to their unreinforced counterparts, indicating that the reinforcement helped maintain the structure's performance over time. For example, CPT20 maintained an efficiency of 0.62 in the first cycle and 0.35 in the fifth cycle, showing better mechanical stability than PT20. *Figure 25* illustrates the force, absorbed energy, and energy absorption efficiency during the loading phase for PT20 and CPT20 in the first cycle. If densification occurs during loading, the

energy absorption efficiency shows a noticeable peak. However, when densification does not happen, the efficiency continues to rise. The CPT20 sample showed no peak in the efficiency curve, while PT20 displayed a distinct peak at approximately 26 mm of deformation, signaling the onset of densification. This figure also clearly demonstrates that the incorporation of carbon fiber significantly increases both the force and absorbed energy levels in the structures.

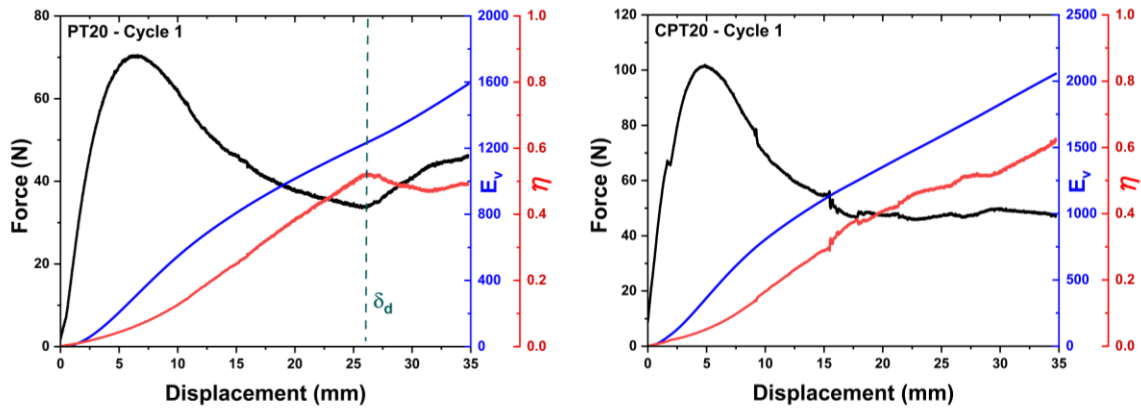


Figure 25: Effect of carbon-fiber reinforcement on densification

Reusability Factor values are presented in *Table 7*, provide insights into the energy absorption performance of the samples.

Table 7: Reusability factors of PT and CPT samples

Sample	Cycle	R_{RF1}	R_{RF2}	Sample	Cycle	R_{RF1}	R_{RF2}
PT10	1	-	-	CPT10	1	-	-
	2	0.77	0.77		2	0.65	0.65
	3	0.43	0.56		3	0	0
	4	0.31	0.71		4	0	0
	5	0	0		5	0	0
PT20	1	-	-	CPT20	1	-	-
	2	0.95	0.95		2	0.82	0.82
	3	0.70	0.73		3	0.67	0.82
	4	0.60	0.85		4	0.46	0.68
	5	0.47	0.78		5	0.32	0.71
PT30	1	-	-	CPT30	1	-	-
	2	0.85	0.85		2	0.83	0.83
	3	0.67	0.79		3	0.67	0.81
	4	0.59	0.88		4	0.55	0.82
	5	0.44	0.75		5	0.50	0.91
PT40	1	-	-	CPT40	1		
	2	0.89	0.89		2	0.81	0.81
	3	0.79	0.90		3	0.65	0.80
	4	0.75	0.95		4	0.49	0.76
	5	0.74	0.98		5	0.44	0.89
PT50	1	-	-	CPT50	1	-	-
	2	1.00	1.00		2	0.99	0.99
	3	0.99	0.99		3	0.97	0.98
	4	0.94	0.95		4	0.94	0.97
	5	0.87	0.93		5	0.88	0.94

The results show that R_{RF1} decreases across all samples as the number of cycles increases, indicating a decline in energy absorption capacity relative to the initial cycle. This reduction is more pronounced in samples with lower TPU content, likely due to their decreased flexibility at room temperature and the potential for localized damage or cracking during programming-recovery cycles. For instance, in PT20, R_{RF1} dropped from 0.95 in the second cycle to 0.47 by the fifth cycle, marking a 51% reduction. In contrast, PT50 showed a smaller decline, decreasing from 1.00 in the second cycle to 0.87 in the fifth cycle, representing a 13% reduction. The addition of carbon fibers further reduces the reusability factor compared to non-reinforced samples. This decrease may stem from localized fiber damage or breakage

during loading, which affects energy absorption in subsequent cycles. Similar to non-reinforced samples, the reusability factor diminishes with an increasing number of cycles, and the reduction is more pronounced in samples with lower TPU content.

In terms of R_{RF2} , which tracks energy absorption changes between consecutive cycles, samples with high TPU content, such as PT50 and CPT50, maintain values close to one. This suggests that their energy absorption capacity remains nearly constant across cycles. On the other hand, samples with lower TPU content, such as PT20, exhibit R_{RF2} values below one, indicating a progressive decline in energy absorption capacity as the cycles continue.

Reusability evaluations revealed a decline in the energy absorption capacity of the structures as the number of cycles increased. This reduction, however, was influenced by the TPU content. Structures with higher TPU content showed a smaller decrease in energy absorption compared to those with lower TPU content, likely due to the reduced ductility of the latter at room temperature, which makes them more susceptible to local damage or cracking and lowers their reusability factor. The addition of carbon fibers slightly reduced the reusability factor, potentially due to localized damage or fiber fractures during loading cycles. Nevertheless, the structures maintained adequate load-bearing capacity and exhibited high shape recovery ratios, affirming their suitability as smart, reusable load-bearing materials.

4.4. Shape Recovery and Shape Fixity Properties of Unit Cell CFRCs

To quantify reusability of the CFRCs, shape recovery and shape fixity ratios are calculated for each cycle. *Figure 26* shows the shape recovery ratios for both unreinforced and carbon fiber-reinforced samples across all programming-recovery cycles, with deformations of 30% and 50%. The data reveals that all samples maintain high shape recovery ratios, exceeding 0.9, even after multiple cycles, underscoring the suitability of the PLA-TPU mixture for 4D printing smart, reusable structures. Additionally, while the inclusion of carbon fiber slightly enhances the shape recovery capability and significantly boosts mechanical properties, the TPU content variation does not notably affect the shape recovery ratio, which remains consistent across all mixtures. *Figure 27* presents the shape fixity ratios of the samples. Unlike the shape recovery ratio, the shape fixity ratio declines as TPU content increases, indicating reduced ability to retain the temporary shape as elastic recovery dominates after unloading.

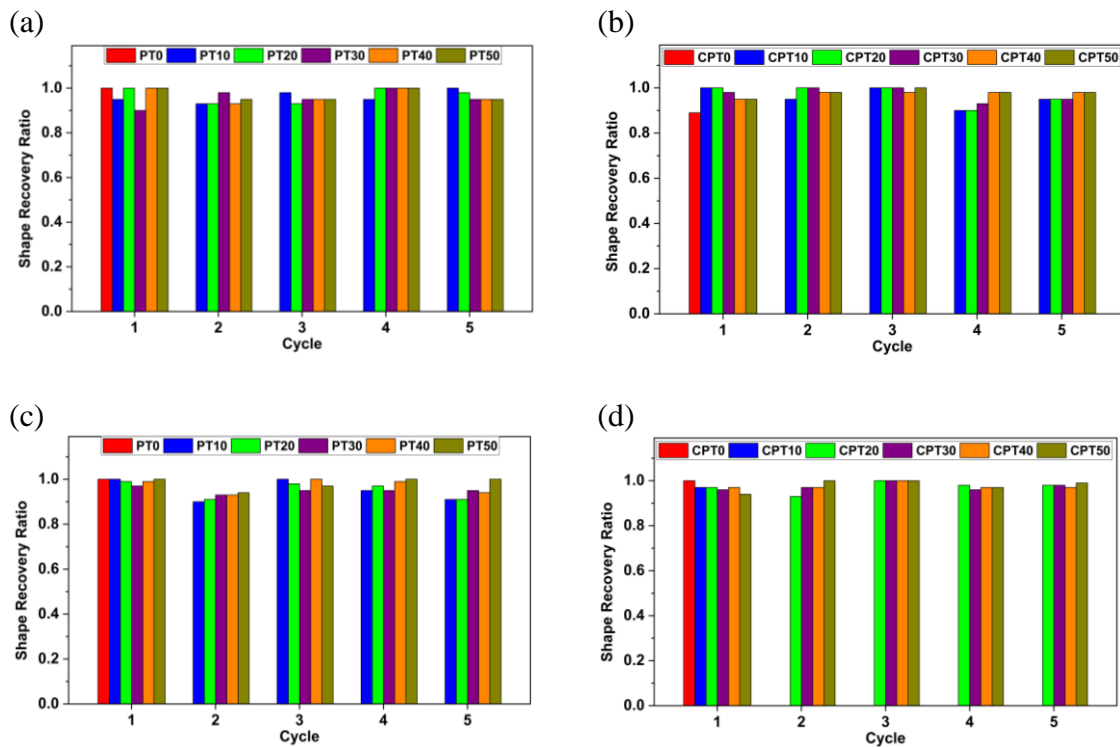


Figure 26: Shape recovery ratio of the samples at different programming deformation, a and b are for 30% deformation, c and d are for 50% deformation

As previously mentioned, the shape recovery ratio of the samples remained largely unaffected by variations in TPU content, but shape fixity affected by TPU ratio majorly. With higher TPU content, elastically recovered length increases after compression. This increase in length decreases shape fixity ratio. When shape fixity ratios are inspected, a non-linear behavior could be seen. This fluctuation arises due to the definition of shape fixity, which assesses the ratio for each cycle independently, without accounting for the influence of consecutive cycles. Also, it is witnessed that shape fixity ratios are highly correlated with storage modulus and damping factors which are obtained from DMA results (*Section 4.1.*). For PT10 and PT20 the storage modulus values are approximately 1200-1250 MPa. And for PT30 and PT40 the storage modulus values are approximately 750-800 MPa. This close variation between consecutive pairs satisfies the similar behavior in shape fixity ratios.

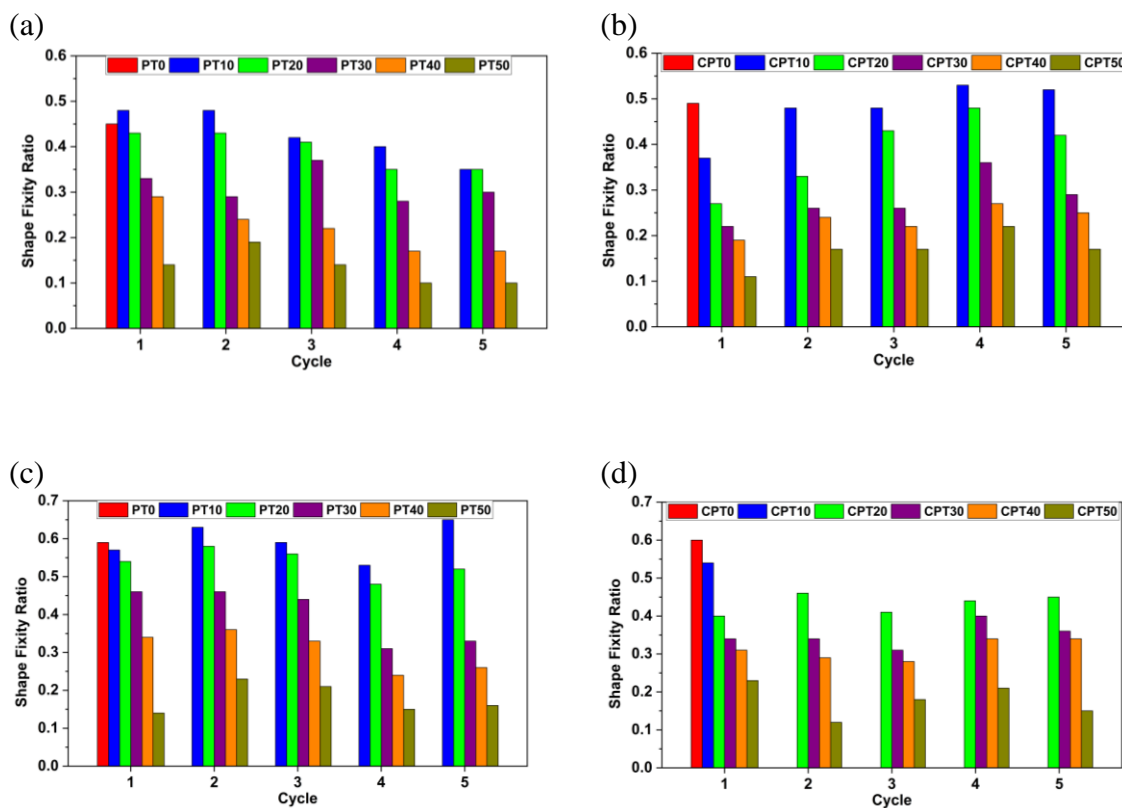


Figure 27: Shape fixity ratio of the samples at different programming deformation, a and b are for 30% deformation, c and d are for 50% deformation

The experiment is repeated two times for PT10, PT20, PT30, CPT10, CPT20 and CPT30 samples under 50% deformation. The shape fixity and shape recovery ratios are examined to verify consistency along with test results. The average shape fixity and recovery ratios and standard deviation bars for 3 repeated tests could be seen in Figure 28.

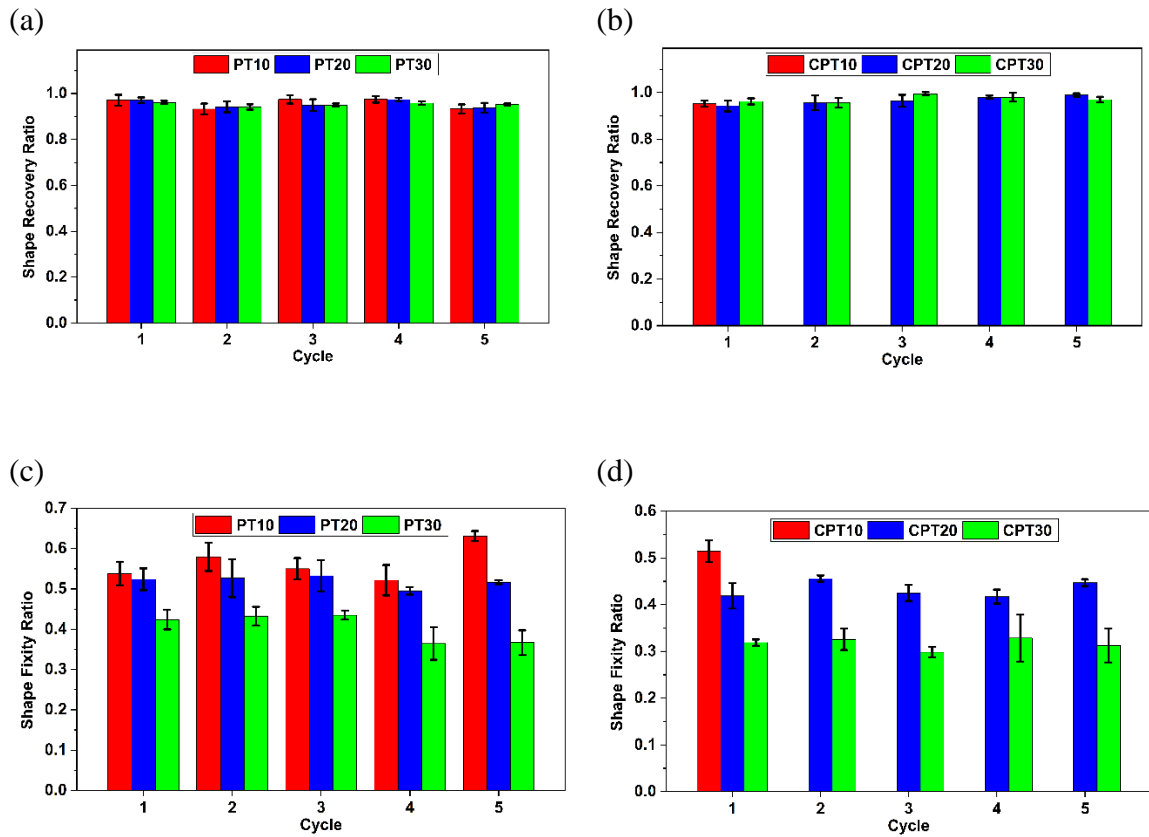


Figure 29: Average shape recovery (a,b) and fixity (c,d) ratios with standard deviation.

5. CELLULAR CFRC STRUCTURES AS REUSABLE ENERGY ABSORBERS

5.1. Re-entrant Cellular Structures as CFRC Energy Absorbers

Auxetic structures possess remarkable properties, including high specific stiffness, strength, and exceptional energy absorption capabilities, which distinguish them from conventional structures. The designs of auxetic structures can be parametrically done to meet the needs of diverse engineering applications. Auxetic materials exhibit a distinctive behavior compared to conventional materials, characterized by their negative Poisson's ratio. This means they shrink laterally under compression and expand laterally under tension, exhibiting deformation that is counter-intuitive to traditional materials (*Figure 30*) [24].

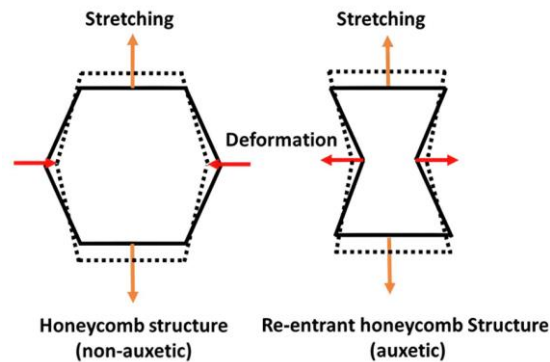


Figure 30: Effect of loading on auxetic and non-auxetic structures [24]

Re-entrant structures, a common form of auxetic architecture, consist of closed polygons defined as an internal angle greater than 180° . This unique configuration enhances the mechanical properties of auxetic structures, particularly their energy absorption capacity. When compressed axially, auxetic structures deform laterally, resulting in a more compact configuration that generates higher stress and greater specific energy absorption. These

characteristics make them highly suitable for use in a range of applications, including personal protective equipment, vibration dampers and isolators [23, 25]. To show benefits of using auxetic structures in CFRCs, inner angles of the cellular structures chosen 70° , 90° , and 110° . These angles help to distinguish effects of the negative Poisson's ratio in terms of mechanical properties.

To show the benefits of using auxetic structures in CFRCs, inner angles of the cellular structures were chosen as 70° , 90° , and 110° . These angles help to distinguish the effects of the negative Poisson's ratio in terms of mechanical properties. The selection of these angles was based on their distinct mechanical responses, particularly in energy absorption, stiffness, and auxetic behavior. According to Choudhry et al. (2023), the re-entrant angle significantly influences the structural performance of cellular materials [24]. A 70° inner angle honeycomb was chosen due to its superior energy absorption capacity, as the reference study indicates that energy absorption peaks around 60° – 70° , providing an effective balance between deformation stability and impact resistance. The 90° brick-like structure was selected for its predictable mechanical behavior, as such configurations exhibit nearly isotropic load distribution without significant lateral expansion or contraction, making them suitable for stable load-bearing applications. Lastly, the 110° outer angle auxetic structure was designed to enhance stiffness while maintaining some auxetic characteristics, as the literature suggests that increasing the re-entrant angle above 100° improves overall mechanical stability [24]. These design choices ensure that each structure serves a distinct functional purpose, optimizing the mechanical performance based on the intended application.

5.2. Energy Absorption Investigation of Cellular CFRCs with Different Inner Angle

Crush Load Efficiency (CLE) and Mean Crushing Load (MCL) values are calculated as discussed in *Section 3.1.* for hexagonal cellular CFRC structures (D70, D90, D110). Compression test cycle for the D70, D90 and D110 could be seen in *Figure 31.*

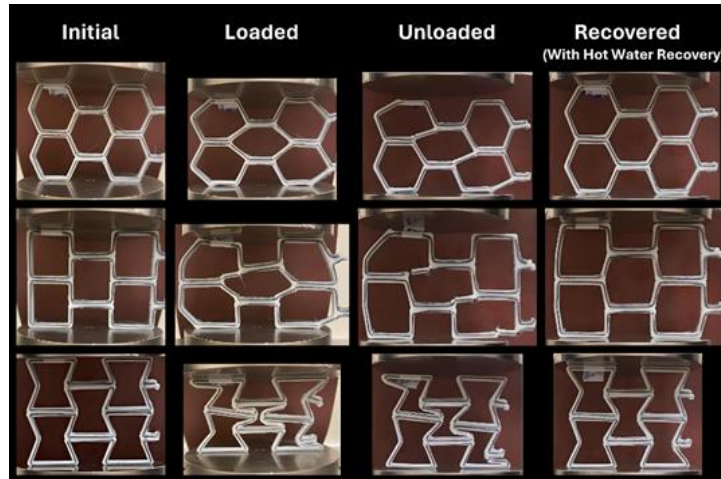


Figure 31: Compression test cycle of D70, D90, D110 CFRCs

It is found that D90 sample has a higher peak force value (IPCF) than the other parts. Because of the brick-like structure, it tolerated high peak loads. But after the compression test, the D90 part failed. In terms of reusability, those parts are insufficient. The auxetic (re-entrant) and the honeycomb-like cellular CFRC structures showed more robust behavior. That property makes them more charming to use as energy absorbers. The results of the compression test, EA, SEA, IPCF, MCL and CLE values could be seen *Figure 32.*

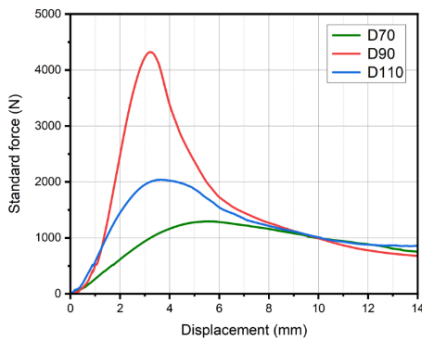


Table 8: Energy absorption calculations for CFRCs

<i>Sample</i>	<i>Mass (g)</i>	<i>EA (J)</i>	<i>SEA (J)</i>	<i>IPCF (kN)</i>	<i>MCL</i>	<i>CLE</i>
D70	27.51	13.30	0.48	1.29	0.92	0.71
D90	32.49	22.49	0.69	4.32	1.56	0.36
D110	35.62	17.50	0.49	2.03	1.22	0.60

Figure 32: Force-Displacement plots of CFRCs and energy absorption calculations

5.3. Path Optimization for Structural Failures

For the hexagonal cellular CFRCs, breakages and imperfections occurred during compression, which resulted from two main factors. The first factor was the displacement of the carbon fiber within the matrix. During printing, as the extruder turned corners, the carbon fiber was pulled, causing it to lose its orientation. The second factor was the disruption in the extrusion flow following the corner turns. Due to the disorientation of the carbon fiber, the extrusion flow was interrupted, leading to a temporary reduction in the amount of PLA material being extruded until the extruder compensate the flow. *Figure 33* presents common breakage locations.

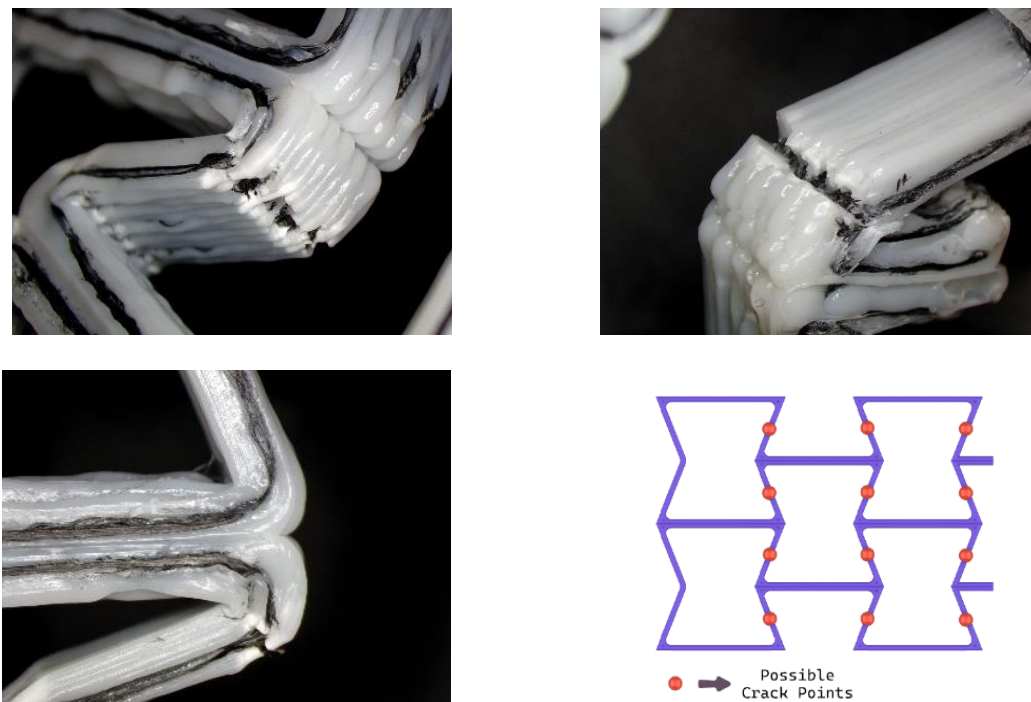


Figure 33: Common breakage locations of loaded auxetic cellular CFRCs

5.4. CFRC Shape Recovery with Hot-water Heating

After evaluating the effects of material composition of CFRCs on cold programming, shape recovery methods are examined.

Hexagonal cellular CFRCs were utilized to evaluate the discussed shape recovery methods. Initially, the deformed samples were subjected to the hot-water recovery method. This process was conducted at a fixed water temperature of 60°C, exceeding the glass transition temperature (T_g) of the PLA filament. The recovery progression of the sample parts over 60 seconds is shown in *Figure 34*.

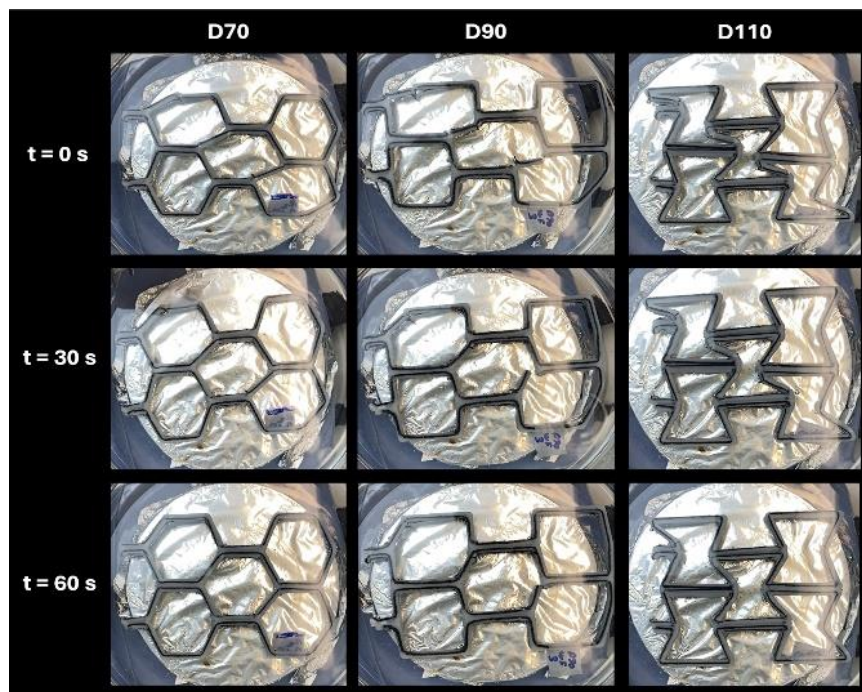


Figure 34: Hot-water recovery of D70, D90 and D110 samples over time

6. ELECTRO-ACTIVE RESPONSES OF CFRCS

6.1. Electro-active Properties of CFRCS

The cellular CFRC samples exhibit continuous conductivity along the printing path. With the designed sample configurations, a parallel circuitry is created, which can function as either a detector or a resistor for heating purposes [12, 13, 49]. Given that the circuitry displays resistive behavior, the impact of mechanical forces on resistance is analyzed. A relationship between absorbed energy and resistance is then established. *Figure 35* illustrates the equivalent circuitry and resistance calculations for one of the samples (D110).

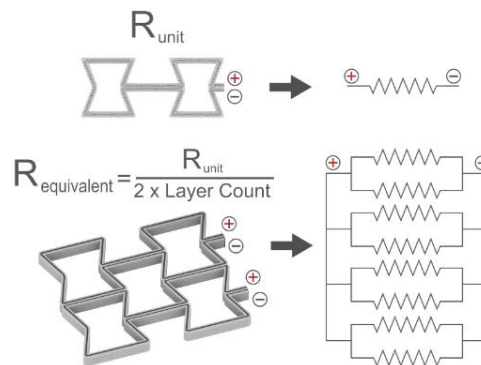


Figure 35: Equivalent circuitry representation of D110 CFRC sample part

As a secondary application, the obtained circuitry is utilized as a semi-co-axial heater. By connecting an external current source, an appropriate current is supplied to the circuitry, and the temperature change is monitored. A Bosch GTC400s thermal camera is used to visualize the heating process. The heating is directly dependent on the applied voltage and time. The designed sample configurations create a parallel circuitry with two resistive lines, which

serves as a resistor for Joule heating [36, 50, 51]. Thanks to the multiport design, the structure can be heated in stages. This staged heating also allows for staged recovery, adding a smart material feature to CFRCs.

To assess the resistive behavior of the CFRC underload, the resistance of the circuitry is measured by connecting points using an Arduino ohmmeter circuit. In this setup, a basic voltage divider is formed, and by reading the voltage values across the resistance, the resistance values are calculated in relation to a reference resistor. The schematic of this circuit is shown in *Figure 36*.

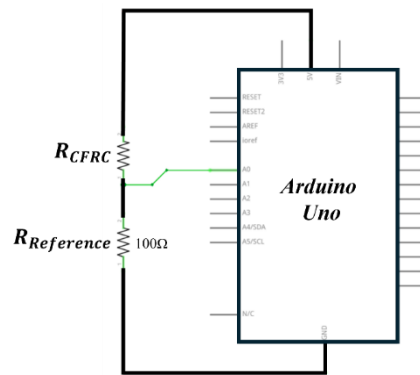


Figure 36: Arduino Uno voltage divider schematic for resistance measurement

6.2. Joule Heating of CFRCs

Subsequently, another set of samples was prepared to investigate the Joule heating method [36, 48-51]. Initially, the impact of various voltage levels was tested on undeformed samples to determine an appropriate voltage for achieving sufficient heating. During these tests, a thermal camera was used to assess heat distribution and uniformity. Additionally, the repeatability and consistency of the thermal behavior were evaluated. Tests conducted at 4V, 8V, 12V, and 16V revealed that a minimum voltage of 16V was required to achieve adequate heating in the undeformed samples. *Figure 37* displays thermal images of the samples heated

with 16V, which supplied 1 to 1.2 A to the circuit and successfully produced sufficient heating.

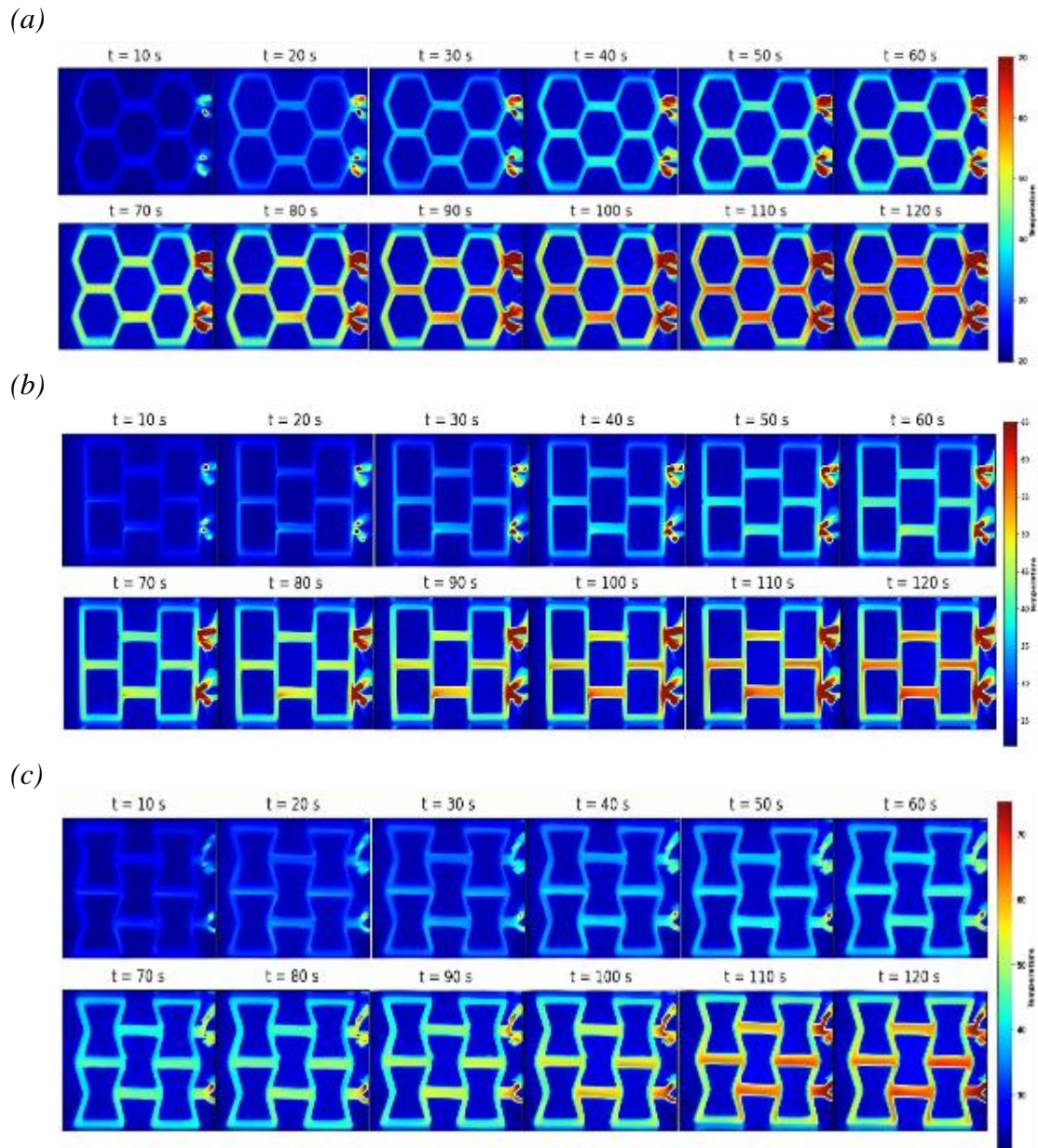


Figure 37: The thermal images of D70 (a), D90 (b), D110 (c) sample parts for 120 seconds

6.3. CFRC Shape Recovery with Joule Heating

The deformed sample parts were also powered with similar currents, and the recovery process was monitored using thermal images. It was found that Joule heating could effectively facilitate recovery through internal heating of the material. However, during compression, local damage disrupted the heat uniformity, although adequate recovery was still achieved. Thermal images of the recovery process are shown in *Figure 38*. The D90 sample was damaged during compression, causing one of the parallel circuits to fail. Nonetheless, the other samples (D70, D110) retained their shape recovery properties. The thermal image of the damaged D90 sample indicated that these structures could be utilized in a sequential heating system, where the heating could be applied stage by stage. Since the electrical circuits in the samples (upper and lower circuits) are connected in parallel, they can either operate simultaneously or be disabled as required.

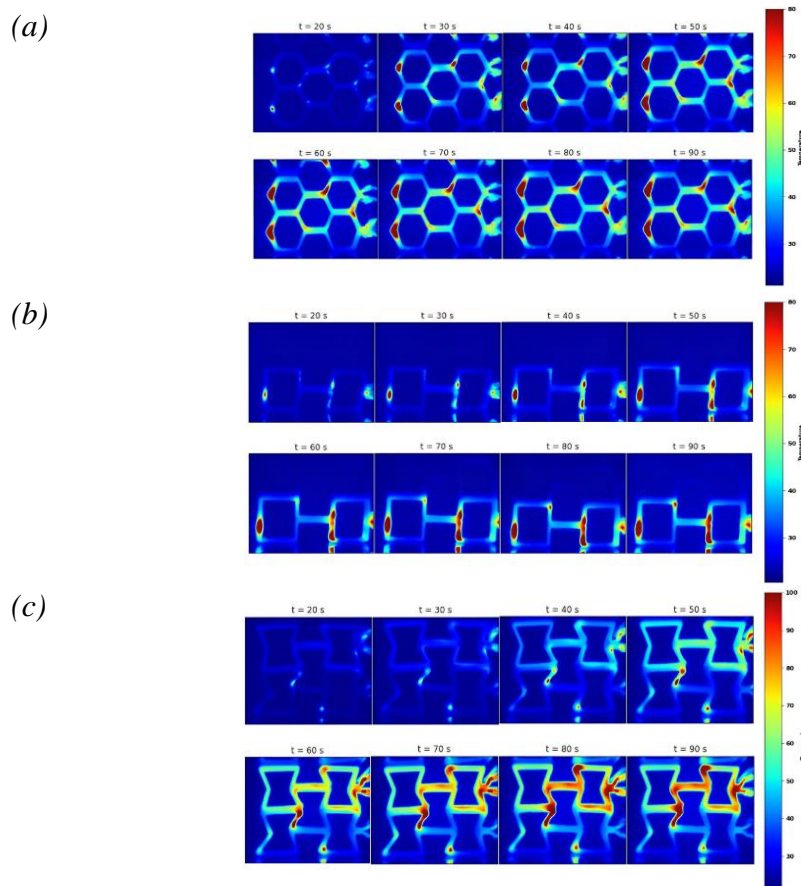


Figure 38: The thermal images of deformed D70 (a), D90 (b), D110 (c) sample parts

The heating uniformity was disrupted, with some hot spots identified in the thermal images, where slightly higher temperatures were recorded. These hot spots were caused by structural damage and indicated the exact locations of the damage. This characteristic is advantageous for using the part as a detector. When comparing the shape recovery ratios, the results showed similar performance between the methods. The Joule heating method achieved a 3-6% higher shape recovery ratio. These results can be seen in *Figure 39*. The Joule heating method heats specific deformed regions in a localized manner due to the increased resistance in those areas. This localized heating explains the difference in shape recovery ratios between hot water recovery and Joule heating. Also, it is witnessed that hot-water recovery was completed between 30-60 seconds depending on the geometry of the structure. On the other hand, recovery with joule heating is completed in around 15-30 seconds. With Joule heating, the deformed regions heated to glass transition (T_g) in a shorter time. This property highlights the multifunctionality of the CFRC.

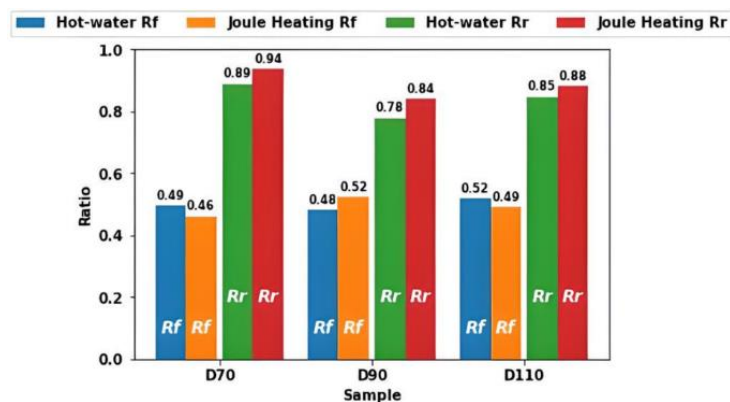


Figure 39: Shape fixity (R_f) and shape recovery (R_r) ratios of D70, D90, D110 CFRCs

6.4. Gradual Joule Heating Concept

To illustrate this concept, a CFRC sample is connected to the power supply in stages. The voltage is fixed at 16V, providing a 1.2 A current. Initially, the first circuit is activated for Joule heating. After 50 seconds, this circuit is turned off, and the second circuit is activated. This experiment demonstrates that staged heating can be achieved with cellular CFRC structures, enabling controllable Joule heating. With this level of control, energy efficiency is optimized through localized stimuli. Thermal images of this experiment are shown in *Figure 40*.

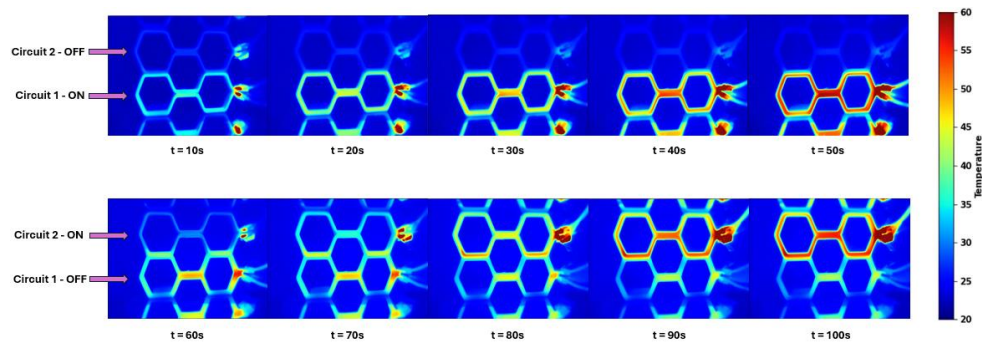


Figure 40: Gradual Joule Heating thermal images of D70 CFRC

6.5. Resistive Sensor Applications of CFRCs

It was observed that the resistance is correlated with deformation caused by external load. As the deformation increases, the resistance values also rise. Once the loading phase is complete and unloading begins, the resistance values stabilize within a similar range. The force-displacement curves along with the resistance values for the D70, D90, and D110 samples are shown in *Figure 41*. Initially, the equivalent resistance values of the samples varied between 25-30 Ohms. The thermal images of the samples supplied with 16 volts which

presented in Section 6.2 show the uniform heat distribution. This result also proves the uniform resistance distribution. As the deformation rate increased, the resistance values exhibited an exponential rise. After the loading phase ended, the resistance values stabilized. In the end, a connection between force, displacement, and resistance was established, enabling the use of resistance measurements for detection purposes. This application highlights the potential of CFRCs as sensors, where real-time resistance measurement can facilitate health monitoring and force detection capabilities.

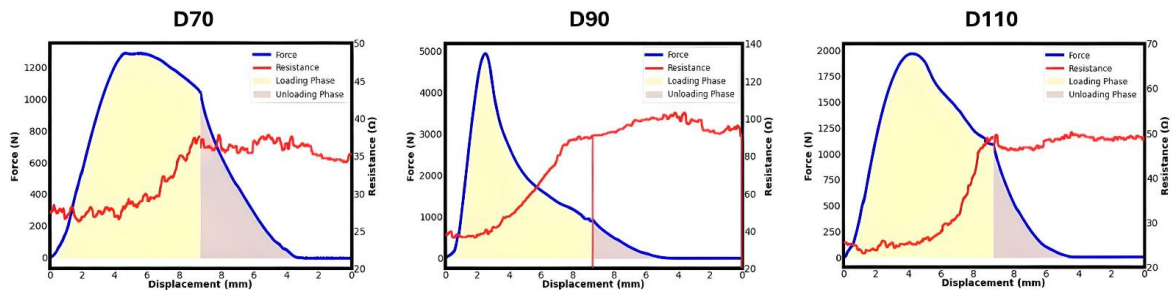


Figure 41: Force-Resistance-Displacement cellular CFRCs under compression

7. CONCLUSION

This thesis aimed to investigate the capabilities of Carbon Fiber Reinforced Composites (CFRCs) in additive manufacturing and 4D response capabilities in advanced applications. Through the systematic achievement of the outlined objectives, the study provides methodology about the integration of CFRCs with 4D printing applications.

In the initial stage of the research, a detailed manufacturing process for continuous fiber-reinforced composites (CFRC) was established, including the design of the machine setup and characterization of materials. This process ensured compatibility with continuous fiber placement and facilitated the fabrication of high-performance composite structures. DSC and DMA tests were conducted to gain a deeper understanding of the co-extruded matrix materials (PLA and TPU). The obtained glass transition (T_g) temperature confirmed that hot water recovery and Joule heating are sufficient for utilizing these materials as smart materials.

The second phase focused on overcoming one of the critical challenges in CFRC fabrication: path planning. Continuous path planning algorithms were successfully implemented for both hexagonal cellular and solid CFRC structures and structural parametrization of the CFRCs established. These algorithms enabled uninterrupted fiber placement. For hexagonal cellular structures, it is shown that the auxetic cellular CFRC (D110) demonstrated superior mechanical performance in terms of energy absorption. In the case of solid CFRCs, the widely recognized plate-with-hole problem was investigated, and three different continuous path planning approaches were evaluated. Overall, different path planning approaches were analyzed and the importance of path planning mechanisms on mechanical behaviors highlighted.

In the final phase, the potential applications of CFRCs in 4D printing were demonstrated. Cold programming is implemented to auxetic unit cell CFRC and hexagonal cellular CFRCs.

The cyclic shape recovery ratio (R_{r_i}) and shape fixity ratio (R_{f_i}) are introduced and effects of co-extruded materials (PLA and TPU) on these ratios are compared. It was observed that samples with higher TPU content demonstrated enhanced shape recovery capabilities after repeated cycles. The findings showed that all PLA-TPU blends achieved high shape recovery ratios exceeding 0.9, highlighting their potential as reusable structures.

One of the notable applications of CFRCs is their potential as reusable energy absorbers. The energy absorption behavior was analyzed for various co-extruded material compositions, revealing that incorporating TPU into the mixtures reduces the softening effect which is a desirable outcome for energy absorbers. However, this improvement comes at the cost of reduced total energy absorption. Achieving a reusable structure with sufficient mechanical properties for load-bearing applications requires an optimal balance of PLA and TPU in the mixture. Increasing TPU content also delayed densification, even under significant deformation. Since densification signals an energy absorber become ineffective, the integration of TPU emerges as a promising development for CFRCs. When compared with the unreinforced samples, carbon fibers in the CFRC slightly reduced reusability, due to localized damage or fiber fractures during loading.

Another application explored was the electroactive behavior of smart CFRC structures. It was demonstrated that CFRCs can function as resistive circuits, serving as either detectors or resistors for heating applications. The relationship between mechanical forces and resistance was examined, revealing that resistance increases linearly with deformation caused by external loads. This characteristic allows resistance measurements to be used for detection purposes. Additionally, gradual heating showcased the controllable capabilities of CFRCs as smart materials, with potential applications in shape recovery via Joule heating. This finding highlights a promising avenue for utilizing CFRCs in advanced applications.

Overall, this thesis shows the current understanding of additive manufacturing by tackling critical fabrication issues and demonstrating the multifunctional capabilities of CFRCs. The findings underline their potential for extensive implementation across various industries, facilitate the way for future innovations in smart material technologies and 4D printing applications. Future work may involve scaling these methods to real-world applications and exploring additional properties of CFRCs to broaden their usability.

8. REFERENCES

1. Ali, H.M.A., M. Abdi, and Y. Sun, *Insight into the mechanical properties of 3D printed strut-based lattice structures*. Progress in Additive Manufacturing, 2023. **8**(5): p. 919-931.
2. Jingcheng, L., et al., *Intelligent polymers, fibers and applications*, *Polymers (Basel)*. 13 (2021) 1427.
3. Kantaros, A. and T. Ganetsos, *From Static to Dynamic: Smart Materials Pioneering Additive Manufacturing in Regenerative Medicine*. Int J Mol Sci, 2023. **24**(21).
4. Lei, M., et al., *Recent progress in shape memory polymer composites: methods, properties, applications and prospects*. Nanotechnology reviews, 2019. **8**(1): p. 327-351.
5. Ngo, T.D., et al., *Additive manufacturing (3D printing): A review of materials, methods, applications and challenges*. Composites Part B: Engineering, 2018. **143**: p. 172-196.
6. Justo, J., et al., *Characterization of 3D printed long fibre reinforced composites*. Composite Structures, 2018. **185**: p. 537-548.
7. Al Abadi, H., et al., *Elastic properties of 3D printed fibre-reinforced structures*. Composite Structures, 2018. **193**: p. 8-18.
8. Dong, K., et al., *Reusability and energy absorption behavior of 4D printed continuous fiber-reinforced auxetic composite structures*. Composites Part A: Applied Science and Manufacturing, 2023. **169**: p. 107529.
9. Dou, H., et al., *Comparative study on in-plane compression properties of 3D printed continuous carbon fiber reinforced composite honeycomb and aluminum alloy honeycomb*. Thin-Walled Structures, 2022. **176**: p. 109335.
10. Hassan, H., et al., *A review of electro-active shape memory polymer composites: Materials engineering strategies for shape memory enhancement*. European Polymer Journal, 2024: p. 112861.
11. Nejatpour, M., A. Fallah, and B. Koc, *Shape Memory PLA/TPU Blend Using High-Speed Thermo-Kinetic Mixing*. ACS omega, 2024.
12. Dong, K., et al., *Electro-induced shape memory effect of 4D printed auxetic composite using PLA/TPU/CNT filament embedded synergistically with continuous carbon fiber: A theoretical & experimental analysis*. Composites Part B: Engineering, 2021. **220**: p. 108994.
13. Fallah, A., et al., *4D printing of continuous fiber-reinforced electroactive smart composites by coaxial additive manufacturing*. Composite Structures, 2023. **316**: p. 117034.
14. Xu, P., et al., *Compression behavior of 4D printed metamaterials with various Poisson's ratios*. International Journal of Mechanical Sciences, 2024. **264**: p. 108819.
15. Fallah, A., Q. Saleem, and B. Koc, *Assessment of mechanical properties and shape memory behavior of 4D printed continuous fiber-reinforced PETG composites*. Composites Part A: Applied Science and Manufacturing, 2024. **181**: p. 108165.
16. Karima, B., M. Habibi, and L. Laperrière, *4D printing of fiber-reinforced auxetic structures: the building blocks: a review*. Smart Material Structures, 2024. **33**(6): p. 063001.
17. Lee, E., *Contour offset approach to spiral toolpath generation with constant scallop height*. Computer-Aided Design, 2003. **35**(6): p. 511-518.

18. Elber, G., E. Cohen, and S. Drake, *CI continuous toolpath generation toward 5-axis high speed machining*. Computer-Aided Design and Applications, 2006. **3**(6): p. 803-810.
19. Matsuzaki, R., et al., *Three-dimensional printing of continuous-fiber composites by in-nozzle impregnation*. Scientific reports, 2016. **6**: p. 23058.
20. Mosleh, N., A.M. Rezadoust, and S. Dariushi, *Determining process-window for manufacturing of continuous carbon fiber-reinforced composite Using 3D-printing*. Materials and Manufacturing Processes, 2021. **36**(4): p. 409-418.
21. Nakagawa, Y., K.-i. Mori, and T. Maeno, *3D printing of carbon fibre-reinforced plastic parts*. The International Journal of Advanced Manufacturing Technology, 2017. **91**(5-8): p. 2811-2817.
22. Li, N., Y. Li, and S. Liu, *Rapid prototyping of continuous carbon fiber reinforced polylactic acid composites by 3D printing*. Journal of Materials Processing Technology, 2016. **238**: p. 218-225.
23. Alomarah, A., et al., *Compressive properties of 3D printed auxetic structures: experimental and numerical studies*. Virtual and Physical Prototyping, 2020. **15**(1): p. 1-21.
24. Choudhry, N.K., B. Panda, and U.S. Dixit, *Energy absorption characteristics of fused deposition modeling 3D printed auxetic re-entrant structures: a review*. Journal of Materials Engineering and Performance, 2023. **32**(20): p. 8981-8999.
25. Chow, L., et al., *3D printing auxetic architectures for hypertrophic scar therapy*. Macromolecular Materials and Engineering, 2022. **307**(5): p. 2100866.
26. Günaydın, K., C. Rea, and Z. Kazancı, *Energy absorption enhancement of additively manufactured hexagonal and re-entrant (auxetic) lattice structures by using multi-material reinforcements*. Additive Manufacturing, 2022. **59**: p. 103076.
27. Lin, C., et al., *Thermal-, magnetic-, and light-responsive 4D printed SMP composites with multiple shape memory effects and their promising applications*. Composites Part B: Engineering, 2024. **274**: p. 111257.
28. Choudhury, S., et al., *Design-encoded dual shape-morphing and shape-memory in 4D printed polymer parts toward cellularized vascular grafts*. Journal of Materials Chemistry B, 2024.
29. Rahmatabadi, D., et al., *4D printing thermo-magneto-responsive PETG-Fe₃O₄ nanocomposites with enhanced shape memory effects*. Applied Materials Today, 2024. **40**: p. 102361.
30. Wang, L., et al., *4D printing of shape-changing structures based on IPN epoxy composites formed by UV post-curing and γ -ray radiation*. Composites Part A: Applied Science and Manufacturing, 2022. **162**: p. 107146.
31. Dayyoub, T., et al., *Shape memory polymers as smart materials: a review*. Polymers, 2022. **14**(17): p. 3511.
32. Lyu, Z., J. Wang, and Y. Chen, *4D printing: interdisciplinary integration of smart materials, structural design, and new functionality*. International Journal of Extreme Manufacturing, 2023. **5**(3): p. 032011.
33. Joseph, A., V. Mahesh, and D. Harursampath, *On the application of additive manufacturing methods for auxetic structures: a review*. Advances in Manufacturing, 2021. **9**(3): p. 342-368.
34. Zhou, X., et al., *Advances in 3D/4D printing of mechanical metamaterials: From manufacturing to applications*. Composites Part B: Engineering, 2023. **254**: p. 110585.
35. Ge, Q., et al., *Multimaterial 4D Printing with Tailorable Shape Memory Polymers*. Scientific Reports, 2016. **6**(1): p. 31110.
36. Roumy, L., et al., *Durability of Joule effect of 3D printed carbon black/polylactic acid: Electrical cyclic tests and analytical modelling*. International Journal of Fatigue, 2023. **173**: p. 107677.

37. Luan, C., et al., *Self-monitoring continuous carbon fiber reinforced thermoplastic based on dual-material three-dimensional printing integration process*. Carbon, 2018. **140**: p. 100-111.
38. Ye, W., et al., *Self-sensing properties of 3D printed continuous carbon fiber-reinforced PLA/TPU honeycomb structures during cyclic compression*. Materials Letters, 2022. **317**: p. 132077.
39. Zhang, H., et al., *Energy absorption diagram characteristic of metallic self-supporting 3D lattices fabricated by additive manufacturing and design method of energy absorption structure*. International Journal of Solids and Structures, 2021. **226**: p. 111082.
40. Nejatpour, M., A. Fallah, and B. Koc, *An overview of 4D printing of smart multifunction continuous fiber-reinforced composites: recent advances and novel applications*. Advanced Composites and Hybrid Materials, 2024. **7**(5): p. 133.
41. Wang, T., et al., *Load-dependent path planning method for 3D printing of continuous fiber reinforced plastics*. Composites Part A: Applied Science and Manufacturing, 2021. **140**: p. 106181.
42. Wang, Q., et al., *Programmable morphing composites with embedded continuous fibers by 4D printing*. Materials & Design, 2018. **155**: p. 404-413.
43. Zhou, Y., et al., *Co-extrusion 4D printing of shape memory polymers with continuous metallic fibers for selective deformation*. Composites Science and Technology, 2022. **227**: p. 109603.
44. Shen, J., et al., *Design and mechanical property studies of 3D re-entrant lattice auxetic structure*. Aerospace Science and Technology, 2021. **118**: p. 106998.
45. Wang, S., et al., *Experimental studies on quasi-static axial crushing of additively-manufactured PLA random honeycomb-filled double circular tubes*. Composite Structures, 2021. **261**: p. 113553.
46. Wang, S. and H.-T. Liu, *Energy absorption performance of the auxetic arc-curved honeycomb with thickness and arc angle gradient based on additive manufacturing*. Materials Today Communications, 2023. **35**: p. 105515.
47. Daniel, F.J., *Characterization of Commercially Available Conductive Filament and Their Application in Sensors and Actuators*. 2021, Louisiana Tech University.
48. Wang, Y., et al., *Electrothermally controlled origami fabricated by 4D printing of continuous fiber-reinforced composites*. Nature Communications, 2024. **15**(1): p. 2322.
49. Tekay, E., *Low-voltage triggered electroactive and heat-responsive thermoplastic elastomer/carbon nanotube polymer blend composites*. Materials Today Communications, 2023. **35**: p. 106443.
50. Lee, Y.C., Y.S. Alsheibly, and M. Nafea. *Joule heating activation of 4D printed conductive PLA actuators*. in *2022 IEEE International Conference on Automatic Control and Intelligent Systems (I2CACIS)*. 2022. IEEE.
51. Tirado-Garcia, I., et al., *Conductive 3D printed PLA composites: On the interplay of mechanical, electrical and thermal behaviours*. Composite structures, 2021. **265**: p. 113744.
52. Beyer, C. and D. Figueroa, *Design and Analysis of Lattice Structures for Additive Manufacturing*. Journal of Manufacturing Science and Engineering, 2016. **138**(12).
53. Held, M., *A geometry-based investigation of the tool path generation for zigzag pocket machining*. The Visual Computer, 1991. **7**: p. 296-308.
54. Khosravani, M.R., et al., *Experimental and numerical investigations of the fracture in 3D-printed open-hole plates*. Theoretical and Applied Fracture Mechanics, 2022. **121**: p. 103543.
55. Zhang, H., et al., *Failure analysis of 3D printed woven composite plates with holes under tensile and shear loading*. Composites Part B: Engineering, 2020. **186**: p. 107835.

56. bin Abdul Jalil, A.M.H., et al., *STRESS BEHAVIOUR OF 3D PRINTED PLATE WITH HOLE*. Journal of Engineering & Technological Advances, 2023. **8**(1): p. 13-29.
57. Liu, X., *On some eigenvalue problems for elastic instabilities in tension*. 2013, University of Glasgow.